Mineralium Deposita
https://doi.org/10.1007/s00126-021-01075-y

ARTICLE

Cu-sulfide mineralogy, texture, and geochemistry in the Tiegelongnan porphyry-epithermal copper system, Tibet, China

Chao Yang[1,2,3] · Georges Beaudoin[2,3] · Ju-Xing Tang[4] · Yang Song[4] · Li-Qiang Wang[4] · Xiao-Wen Huang[5]

Received: 28 July 2020 / Accepted: 29 August 2021

Abstract

The Tiegelongnan porphyry-epithermal deposit (2089 Mt @ 0.53% Cu, 0.08 g/t Au) is host to a large variety of Cu-sulfide minerals, mainly chalcopyrite, bornite, covellite, digenite, enargite, and tennantite. We used LA-ICP-MS to investigate the trace element geochemistry of the Tiegelongnan Cu-sulfides, as well as pyrite, to understand the correlation between sulfides and trace elements, gold in particular, in the porphyry and epithermal systems. Porphyry mineralization consists of stage 1 chalcopyrite-pyrite ± molybdenite, stage 2 chalcopyrite-bornite, and stage 3 covellite. Epithermal sulfides form stage 4 pyrite-alunite, stage 5 digenite-bornite-chalcopyrite, and stage 6 enargite-tennantite ± tetrahedrite. Stage 2 chalcopyrite (S2 Ccp, median = 9.7 ppm Au) is the primary porphyry Au host, and stage 6 tennantite in alunite veins (S6 Tnt-s, median = 98.0 ppm Au) is the major epithermal Au host. These Au-rich sulfides formed under higher oxidation conditions, suggesting that a high oxidation state favors the incorporation of Au in Cu-sulfides. Gold contents in coeval chalcopyrite and bornite are positively correlated to temperature, and Au is enriched in chalcopyrite over bornite at low temperatures (< 350 ℃). Positive correlations between Au and As and Te in covellite and chalcopyrite result from the reaction of $As^{3+} + (Au^{+}/Ag^{+}) + Te^{2-} \leftrightarrow 4Cu^{+} + S^{2-}$. Epithermal chalcopyrite and bornite contain more As and Pd than that in porphyry stages, and high contents of As, Sn, Cd, Zn, Sb, Te, Au, and Bi in epithermal enargite and tennantite are likely the result of partitioning of these elements in sulfides at low epithermal temperatures. Epithermal overprinting likely leached Cu from earlier porphyry stage sulfides to precipitate high Cu-grade epithermal mineralization. The Cu-sulfides and related trace elements show a spatial distribution, potentially useful for the exploration of overprinted porphyry-epithermal systems.

Keywords Cu-sulfide · Trace element · LA-ICP-MS · Gold · Porphyry · Epithermal

Introduction

Several studies of sulfide texture and trace element geochemistry have focused on pyrite in porphyry and epithermal deposits (Huston et al. 1995; Reich et al. 2013; King et al. 2014; Rottier et al. 2016; Sykora et al. 2018). Copper-bearing sulfide assemblage zonation and replacement are found in porphyry-epithermal Cu-Au systems (Sillitoe 1999; Garza et al. 2001; Ossandón et al. 2001). However, the trace element geochemistry of Cu-bearing sulfides has rarely been studied in detail. A few studies have focused on enargite geochemistry, and found it to be a significant carrier of Fe, Zn, Sb, Sn, Te, Ge, and Bi (Deyell and Hedenquist 2011; Maydagán et al. 2013; Rottier et al. 2018; Liu et al. 2019). Enargite and other Cu-sulfides, such as covellite, digenite, bornite, and chalcopyrite, can host economically critical metals, and/or high contents of Au and Ag, as valuable by-products in porphyry deposits (Simon et al. 2000; Kesler

Editorial responsibility: P. Hollings.

✉ Chao Yang
chaoyangcn8@gmail.com

1 College of Earth Science, Chengdu University of Technology, Chengdu 610059, China

2 Département de Géologie et de Génie Géologique, Université Laval, G1V 0A6 Québec, Canada

3 Centre de Recherche sur la Géologie et l'ingénierie des Ressources Minérales (E4m), Québec, Canada

4 MLR Key Laboratory of Metallogeny and Mineral Assessment, Institute of Mineral Resources, Chinese Academy of Geological Sciences, Beijing 100037, China

5 State Key Laboratory of Ore Deposit Geochemistry, Institute of Geochemistry, Chinese Academy of Sciences, Guiyang 550081, China

Published online: 20 September 2021

et al. 2002; Reich et al. 2010; Crespo et al. 2018; Liu et al. 2019). The reasons for the relationship between trace elements and Cu-sulfides remain the subject of debate.

The Tiegelongnan deposit, Tibet (China), is a well-developed hydrothermal system with high-sulfidation epithermal Cu (Au) mineralization overprinting an older porphyry Cu (Au) mineralization (Yang et al. 2020a, b; Zhang et al. 2020). The abundance and spatial distribution of Cu-sulfides, including Cu-Fe-S, Cu-S, and Cu-As-S minerals, described at Tiegelongnan (Yang et al. 2014; He et al. 2018; Wang et al. 2018), provide an ideal example to investigate the trace element geochemistry of Cu-sulfides in an overprinted porphyry-epithermal copper system. This study investigates the sulfide mineralogy, textures, using reflected-light microscopy, scanning electron microscope (SEM), and in situ mineral geochemistry combining electron probe microanalysis (EPMA) and laser ablation inductively coupled plasma-mass spectrometry (LA-ICP-MS) analyses. We establish the trace element-Cu-sulfide relationships, focusing on gold-Cu-sulfide correlations, as gold is an important by-product of the Tiegelongnan deposit. The influence of metal substitution mechanisms, physicochemical conditions, and hydrothermal fluid overprinting on Cu-sulfides geochemistry are discussed to improve our understanding of the formation and exploration of overprinted porphyry-epithermal deposits.

Geology

Regional geological background

The Bangong-Nujiang Suture Zone (BNSZ) is a > 1200 km long west-east belt, comprising Jurassic to Cretaceous flysch, mélange, and ophiolitic fragments, interpreted to be remnants of the Bangong-Nujiang ocean (BNO) between the Lhasa and Qiangtang terranes in central Tibet (Fig. 1A; Yin and Harrison 2000; Pan et al. 2012). Extensive Jurassic and Cretaceous continental arc-related magmatic rocks were emplaced both in the Qiangtang and Lhasa terranes and in the suture zone (Fig. 1A; Li et al. 2014; Zhu et al. 2016). Those igneous rocks are associated with the long-lived subduction of the BNO and collision between Qiangtang and Lhasa from ~ 170 to ~ 100 Ma (Zhang et al. 2012; Liu et al. 2014; Li et al. 2018). Several porphyry-related deposits are related to the emplacement of the Jurassic and Cretaceous intrusions (Fig. 1A), including the Jurassic Fuye and Caima skarn Fe (Cu) deposits formed between 165 and 153 Ma, the Early Cretaceous Duolong district, Qingcaoshan, and Bainong Early porphyry Cu-Au deposits formed at ~ 120 Ma, and the Late Cretaceous Gaerqiong-Galale and Balaza porphyry-skarn Cu-Mo deposits formed at ~ 90 Ma (Zhang et al. 2015; Li et al. 2017a).

The Duolong district is located in the southern Qiangtang terrane, around 30 km to the north of the BNSZ (Fig. 1A). There are several porphyry and epithermal Cu-Au deposits in the district (Fig. 1B). The bedrock of the Duolong district consists of the Upper Triassic Riganpeicuo Formation limestone, overlain by the Upper to Middle Jurassic Sewa and Quse formations sandstone, siltstone, and claystone. The Sewa and Quse formations were intruded by syn-mineralization Cretaceous porphyritic intrusions, and are overlain by post-mineralization Cretaceous volcanic rocks. The Oligocene Kangtuo Formation conglomerate and Quaternary eluvial-diluvial sediments both unconformably overlie the Jurassic sedimentary and Cretaceous volcanic rocks (Fig. 1B).

The porphyritic intrusions are intermediate to felsic, including diorite, quartz diorite, and granodiorite, crystallized from oxidized, water-rich, and continental arc-related calc-alkaline magmas that intruded between 126 and 116 Ma (Li et al. 2016, 2017b; Lin et al. 2017a; Sun et al. 2017). Volcanic rocks spatially associated with these porphyritic intrusions in the Duolong district (Fig. 1B) consist of basalt, andesite, dacite, rhyolite, and voluminous pyroclastic rocks, erupted between 114 and 105 Ma (Wang et al. 2015; Li et al. 2016; Wei et al. 2017).

The Tiegelongnan deposit

The Tiegelongnan deposit is the largest deposit within the Duolong district, with resources of 2089 Mt grading 0.53% Cu (Jinlong Mining Co., Ltd, 2017), and 0.08 g/t Au (Tang et al. 2017). It was the first high-sulfidation epithermal mineralization, telescoped on a porphyry deposit, discovered in Tibet (Tang et al. 2014). Detailed geology, exhumation, and preservation history from ~ 120 to ~ 110 Ma have been described in several earlier studies (Lin et al. 2017a, b; Song et al. 2018; Zhang et al. 2018, 2020; Yang et al. 2020a, b). The exposed bedrock at the surface of the Tiegelongnan deposit consists mostly of Cretaceous andesite (Fig. 2A), such that the deposit geology is known from diamond drill cores. Several pulses of porphyritic dikes intruded the Jurassic sandstone of the Sewa Formation, which is metamorphosed to hornfels below a depth of ~ 1000 m (Fig. 2B). A diorite porphyry to the east (Fig. 2B) is a pre-mineralization intrusion, dated at ~ 123 Ma (Lin et al. 2017b). Earlier studies reported that the granodiorite porphyry was the syn-mineralization intrusion, as the Tiegelongnan hydrothermal system was centered on the granodiorite porphyry dikes, and yielded a similar age to molybdenite of ~ 120 Ma (Fang et al. 2015; Lin et al. 2017a; Zhang et al. 2018). Yang et al. (2020b), however, recognized several different granodiorite porphyry phases based on their petrology, and dated phases 1, 2, and 3 at an age of ~ 120 Ma, whereas phase 4 yielded an age of ~ 116 Ma. Hydrothermal biotite and muscovite

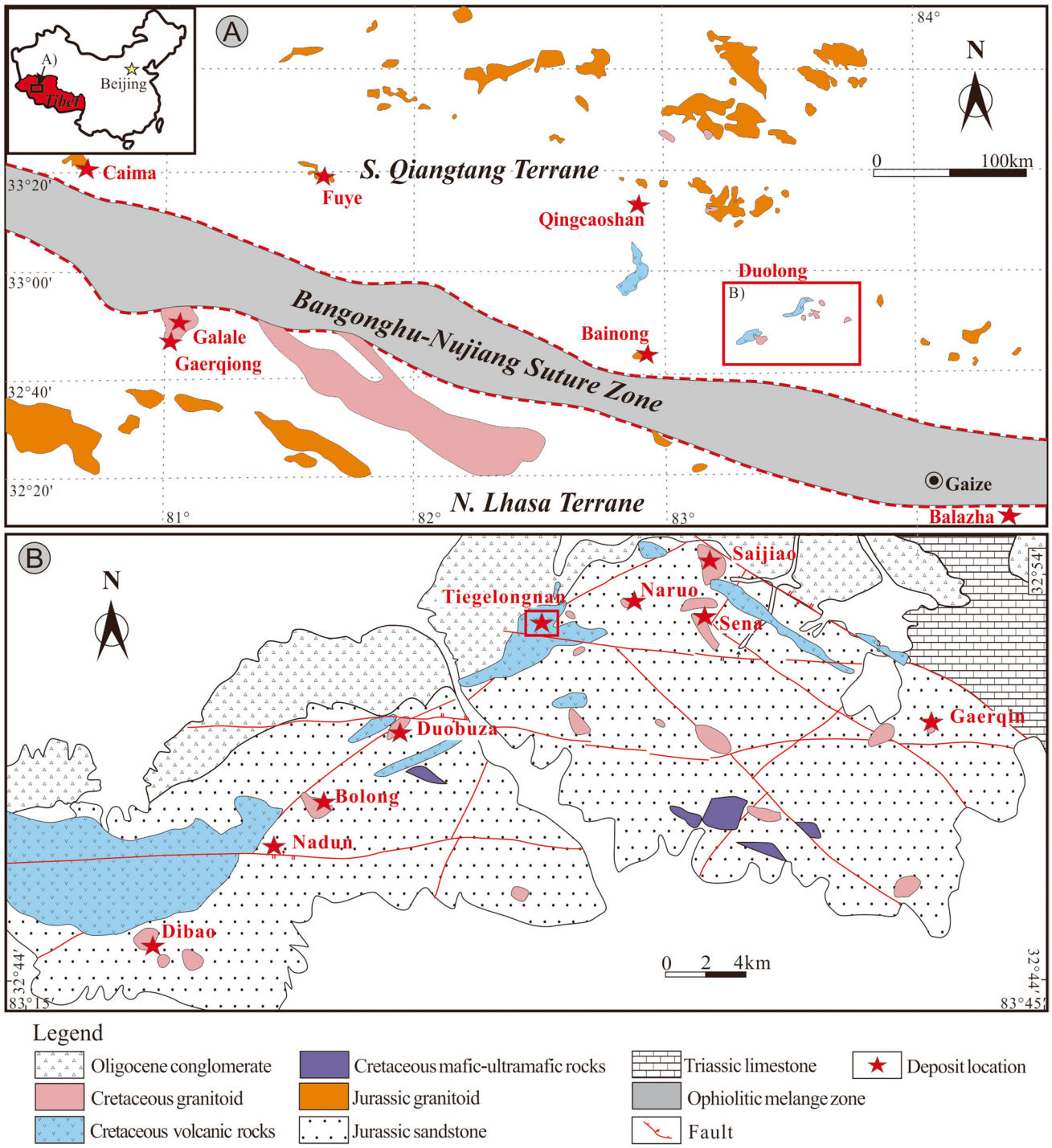

Fig. 1 Regional geology of the western Bangong-Nujiang suture zone (**A**), modified after Zhu et al. (2016). The Duolong porphyry deposits district (**B**), modified after Lin et al. (2017a)

alteration (Figs. 2B and 3) were dated at around ~ 120 Ma (Lin et al. 2017b; Yang et al. 2020b), suggesting that the hydrothermal alteration facies are likely genetically associated with granodiorite porphyries 1, 2, and 3.

The biotite alteration consists of rare early biotite (EB), and barren quartz veins, which are cut by later quartz-molybdenite ± chalcopyrite ± pyrite (B1) veins and quartz-chalcopyrite-bornite (A) veins. Chlorite-pyrite-quartz veins (C veins in Zhang et al. 2018, 2020) occur in the chlorite alteration zone, locally having minor amounts of chalcopyrite. Chalcopyrite, pyrite, and molybdenite in biotite and chlorite alteration zones form stage 1 sulfides (Fig. 3).

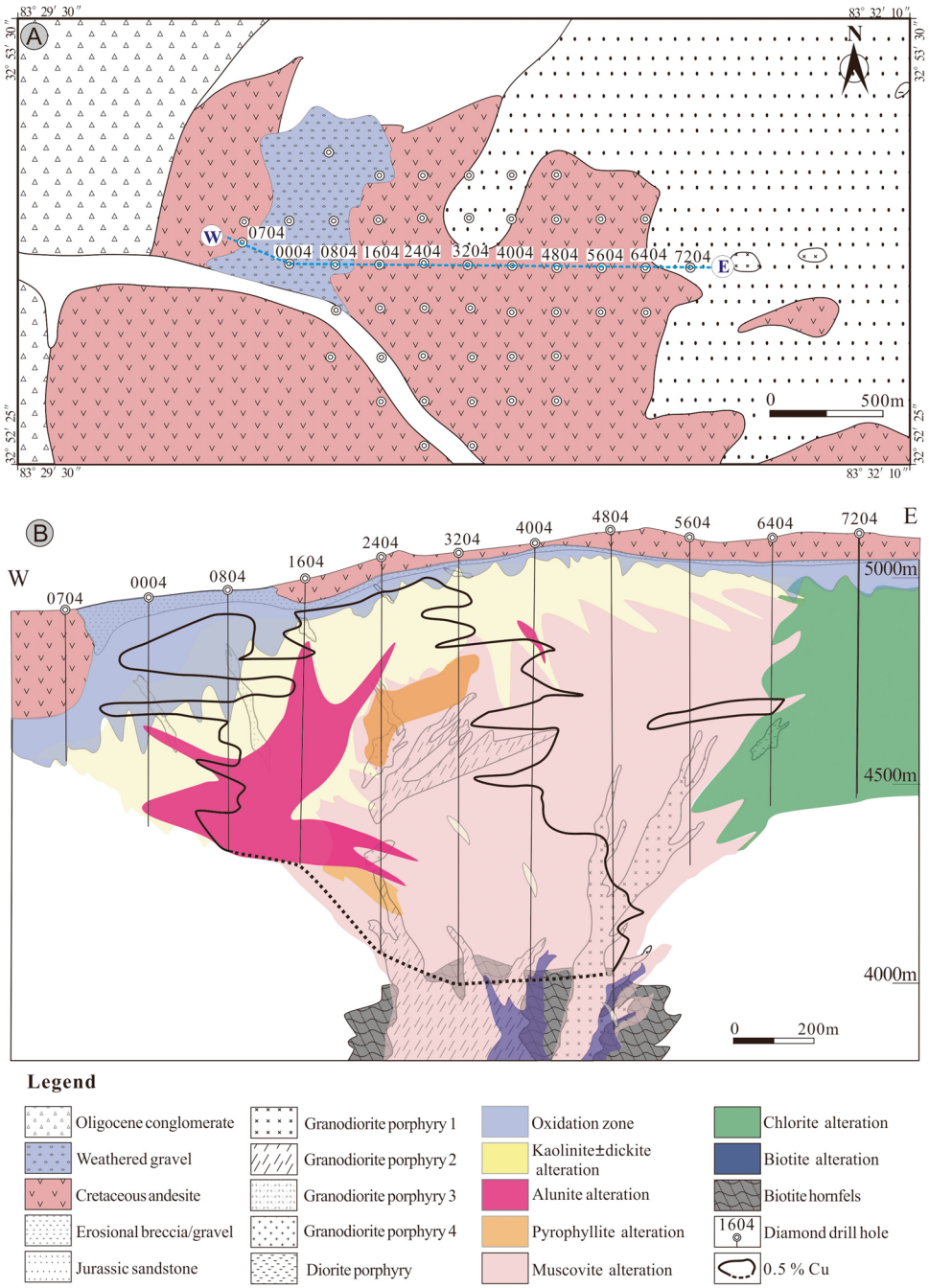

Fig. 2 Geology of the ground surface (**A**) and EW cross-section (**B**) at the Tiegelongnan deposit, modified after Yang et al. (2020b)

Muscovite alteration hosts most porphyry Cu, comprising stage 2 bornite-chalcopyrite and stage 3 covellite (Fig. 3). Quartz-chalcopyrite-bornite (A), quartz-molybdenite (B2), quartz-pyrite (D), and pyrite veins are present in the muscovite alteration zone. Anhydrite and gypsum are found in D veins, which were termed as "late-stage veins" by Zhang et al. (2018, 2020). Pyrophyllite and dickite patches are disseminated in the muscovite zone (Fig. 2B).

Porphyry hydrothermal alteration and mineralization were subsequently overprinted by epithermal alunite and kaolinite-dickite alteration at the top and western parts of the deposit (Fig. 2B). Yang et al. (2020a, b) recognized two epithermal events, including the early event at ~ 116 Ma associated with alunite I, and a late event at ~ 112 Ma, associated with alunite II and kaolinite I. The early epithermal event has a minor amount of Cu-sulfide, whereas the ~ 112 Ma epithermal event contributes to the major epithermal Cu (Au) mineralization (Fig. 3). The late epithermal event includes three sulfide stages, stage 4 pyrite-alunite, stage 5 bornite-digenite-chalcopyrite, and stage 6 enargite-tennantite (Fig. 3). Other types of kaolinite (type II filling quartz veins and type III filling alunite

Stage	Event/alteration	Age (Ma)	Sulfide paragenesis	Copper percentage	Intrusion depth	Overprinting
Post-mineralization	Alunite Ⅳ	100.6±2.0[3]				
	Supergene		Chalcocite, covellite, digenite, native Au, Cu	10		
	Andesite	110.1±0.7[1]				
	Kaolinite Ⅱ,Ⅲ					
	Alunite Ⅲ	112.5±0.8[3]				
Late epithermal	Alunite Ⅱ-kaolinite Ⅰ	111.7±1.0[3]	S6:enargite-tennantite, S5:bornite-chalcopyrite -digenite S4:pyrite-alunite	50		
Early epithermal	Alunite Ⅰ	116.3±0.8[3]	Pyrite-enargite	2		
Porphyry	Muscovite	120.9±0.8[3]	S3: covellite S2: chalcopyrite-bornite	25		
	Chlorite		S1: Pyrite±chalcopyrite	3		
	Biotite	121.1±0.6[2]	S1: chalopyrite-pyrite -molybdenite	10		

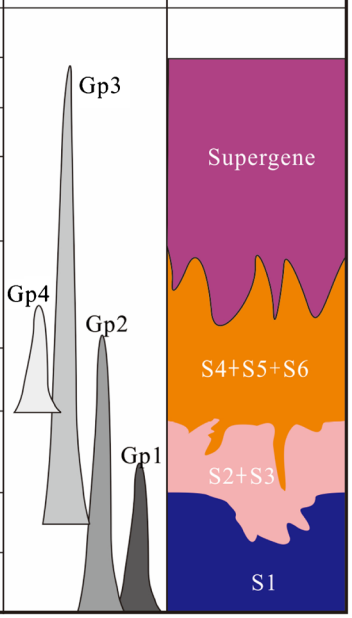

Fig. 3 Magmatic-hydrothermal sequences and overprinting relationships at the Tiegelongnan deposit. 1-Wang et al. (2015); 2-Lin et al. (2017a); 3-Yang et al. (2020b)

veins) are post-mineralization events (Fig. 3; Yang et al. 2020a).

During and after the formation of the overprinted porphyry-epithermal hydrothermal system, the Tiegelongnan deposit was unroofed during compressive uplifting and paleosurface subsidence, prior to being covered by post-mineralization andesite at around 110 Ma (Figs. 2B and 3; Wang et al. 2015; Lin et al. 2017b). A thin layer of oxidized capping and erosional breccia/gravel occurs at the top of the erosional surface, beneath the andesite cover (Figs. 2B and 3). Pyrite in shallow veins is oxidized to hematite and other hydrous Fe-oxides. Supergene chalcocite ± digenite ± pyrite, native copper, and Cu-oxide veins are found within and beneath the oxidization zone, contributing to small amounts of supergene copper enrichment at Tiegelongnan (Fig. 3).

Methods

More than 150 core samples, representative of deep porphyry to shallow epithermal mineralization zones, were collected to prepare thin sections to study the sulfide mineralogy and textures. The early epithermal event contains minor Cu-sulfides, which were not investigated because grain size is too small for LA-ICP-MS trace element analysis. The thin Sects. (62) were examined using an optical microscope and then 19 representative samples with large sulfide grains were selected for detailed imaging and geochemical analyses. The Inspect F50 scanning electron microscope (SEM, Université Laval) and backscattered electron (BSE) imaging were used to document sulfides textures and micro-scale inclusions. The SEM is equipped with an EDAX's Octane super-A model Energy Dispersive Spectrometer (EDS) to analyze the composition of inclusions.

EPMA

Hypogene sulfides were analyzed for major and minor elements, including S, Fe, Co, Cu, Zn, As, Sn, Sb, and Pb contents at Université Laval using a CAMECA SX-100 electron probe microanalyzer (EPMA), equipped with five wavelength-dispersive spectrometers. A 5-µm-diameter beam with a voltage of 15 kV and a current of 100 nA was used for analysis. Different standards for those major and minor elements (Marx for S, Magx for Fe, Chalco for Cu, Co-ATX for Co, Sphal for Zn, GaAs-ATX For As, Cassit for Sn, Sb-ATX for Sb, and Gal for Pb) were used to calibrate the EPMA data, which is in Electronic Supplementary Materials (ESM) 1 Table S1.

LA-ICP-MS

Trace elements were analyzed by laser ablation inductively coupled plasma-mass spectrometry (LA-ICP-MS) at

LabMaTer, Université du Québec à Chicoutimi (UQAC), using an Excimer 193 nm Resonetics Resolution M-50 laser ablation system coupled with an Agilent 7700 × mass spectrometer. A range of beam sizes were used from 33 to 75 µm with 20 s baseline and 30–40 s of laser ablation, and all data were collected from line scan across sulfide grains polished surfaces. Line locations were selected to avoid visible inclusions. Analytical conditions are similar to those in Duran et al. (2015) and Genna and Gaboury (2015). Maps of the semi-quantitative element distribution in sulfides used a beam size 11–15 µm and stage speed 30 µm/s. A laser frequency of 15 Hz and a power of 5 MJ/ pulse were used to map the sulfides. Data reduction was carried out using the Iolite package running Igor Pro software (Paton et al. 2011). Multiple sections of signal selection were conducted in some samples with peak LA-ICP-MS signals to avoid including inclusions in the results. Internal standardization for pyrite, chalcopyrite, and bornite was based on Fe contents, whereas for digenite, covellite, enargite, and tennantite, it was based on S contents from EMPA results. All sulfide data were calibrated with reference material MASS-1 (Wilson et al. 2002). Another reference material, Laflamme Po727, which is a synthetic FeS doped with 40 ppm PGE and Au supplied by the Memorial University of Newfoundland, was used to calibrate for PGE. GSE, UQAC-FeS-22, and JB-MSS5 reference materials are used for intra-standard quality control. The results of LA-ICP-MS analyses were generally within 10% relative standard deviation (RSD) of the working values of GSE, UQAC-FeS-22, and JB-MSS5 (ESM 1 Table S2).

Multivariate statistical analysis

Partial least squares-discriminant analysis (PLS-DA) was applied to investigate the compositional relationship between different sulfides in porphyry and epithermal mineralization stages, based on the methods described in Makvandi et al. (2016b) and Huang et al. (2019). PLS-DA is a supervised classification technique using labeled data. The censored data (below detection limit) was substituted using the robCompositions R-package, where the k-nearest neighbors (impKNNa) function was used to impute censored values using the Aitchison distance (Makvandi et al. 2016a). Imputed censored data were transformed using the centered-log ratio (Makvandi et al. 2016a), a symmetric transformation with an orthonormal basis (Egozcue et al. 2003). Manganese, Ni, and Pd were not included in the PLS-DA because over 40% of the data for these elements in one mineral was below the detection limit. In terms of interpretation of the PLS-DA data, the PLS-DA loadings (qw^*_1-qw^*_2) and score scatter plots (t_1-t_2) are combined to show the correlation among elements and sulfide minerals. Elements plotting in the vicinity of each other in PLS-DA loadings space have positive correlations, and they are negatively correlated to those in the opposite quadrant. Data plotting close to the origin of score scatter plots (t_1 and t_2) represent the mean composition of the whole data set, such that sulfides plotting close to the origin are not well discriminated by the PLS-DA. Score contribution plots depict the compositional difference between the mean composition of one sulfide and the mean composition of the whole data set (Makvandi et al. 2016b).

Results

Sulfide mineralogy and textures

Detailed core logging and reflected-light microscopy, based on average abundance from 2 to 5 polished thin sections from each investigated site, were used to define the Cu-sulfide spatial distribution (Fig. 4). Combined with SEM analyses for selected thin sections, sulfide assemblages, textures, and inclusions are characterized (Figs. 5 and 6). Porphyry mineralization forms three sulfide stages. Stage 1 chalcopyrite (S1 Ccp) occurs mostly as disseminated grains with pyrite (S1 Py), and locally with molybdenite, within B1 veins, at depths of 1000–1200 m in the eastern part of the EW-04 cross section close to the biotite alteration zone (Figs. 2 and 4). The second stage sulfide assemblage comprises chalcopyrite (S2 Ccp) and bornite (S2 Bn) intergrown with each other (Fig. 5A), at intermediate depths between 500 and 1000 m, in A veins and disseminated in muscovite alteration (Fig. 4). Disseminated S2 Ccp and Bn are more abundant than those in A veins. The two minerals precipitated after S1 Py, filling fractures and voids in S1 Py, or mantling its rims (Fig. 5A and B). Galena inclusions occur in S2 chalcopyrite and bornite, surrounding and filling S1 pyrite fractures (Figs. 6A and B). Hypogene covellite (S3 Cv) characterizes the third sulfide stage, at depths from 300 to 1100 m in the center of Tiegelongnan (Figs. 3 and 4), where it replaces S2 bornite and chalcopyrite (Fig. 5B and C).

Sulfide stages 4, 5, and 6 form the younger epithermal event. Stage 4 is characterized by pyrite that precipitated with alunite (Fig. 5E). Later S5 bornite-digenite surrounds stage 4 pyrite (S4 Py), and the voids and fractures in pyrite are filled by later S6 tennantite (Fig. 6H). The fifth stage sulfide assemblage consists of digenite (S5 Dg), bornite (S5 Bn), and chalcopyrite (S5 Ccp; Fig. 3), which occur at shallow depths of 300–500 m in the overprinting zone between the muscovite and alunite-kaolinite-dickite alterations (Figs. 2 and 4). Stage 5 Dg replaces S3 Cv (Fig. 5D), although these two minerals were considered to have formed simultaneously in earlier studies at Tiegelongnan (He et al. 2018; Wang et al. 2018; Zhang et al. 2018). Stage 5 digenite is commonly intergrown with S5 Bn in disseminated grains (Figs. 5H), but it does not occur with S5 Ccp.

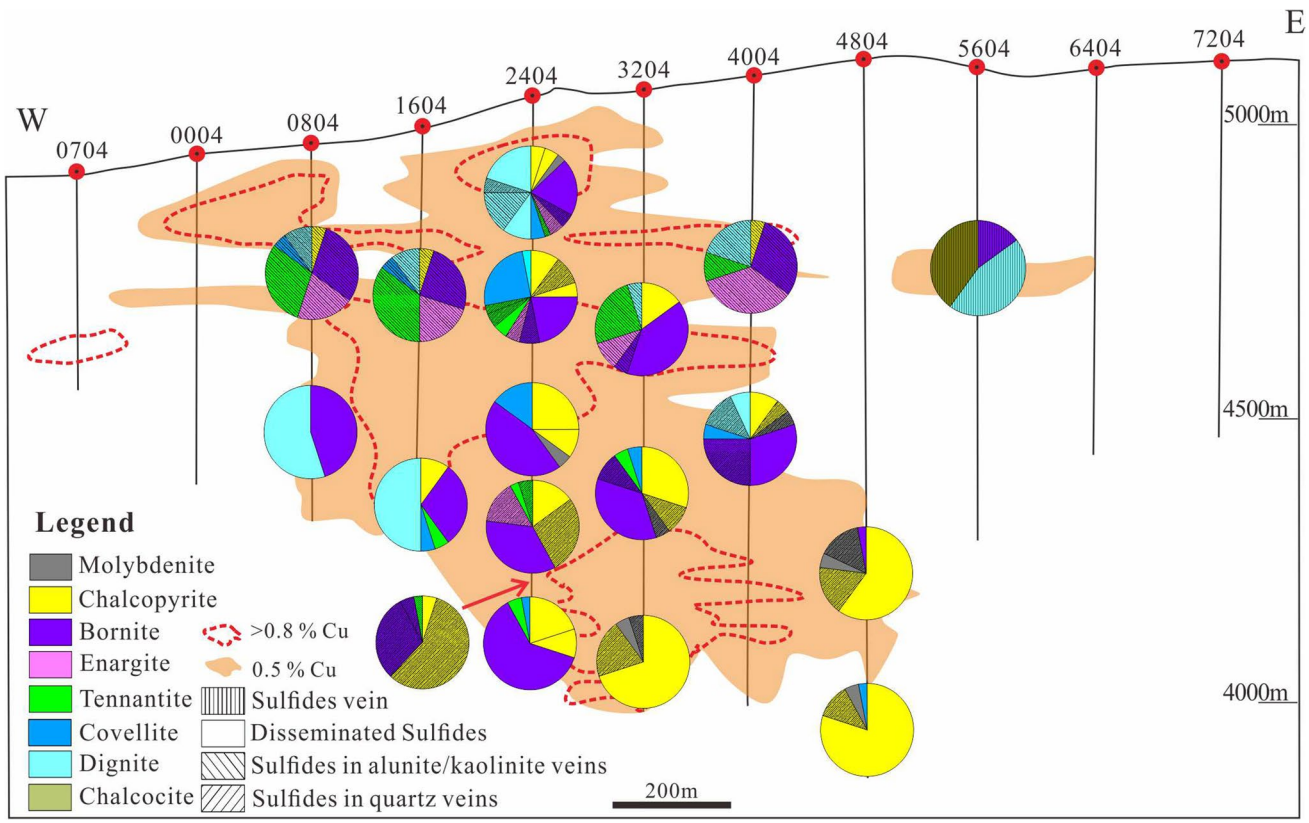

Fig. 4 Distribution of Cu-sulfides in the EW cross-section, estimation from microscope observation of 2 to 5 polished thin sections at each location

A small amount of S5 Bn and Dg replace S1 Py in D and pyrite veins. Galena inclusions are found in S5 Dg and Bn (Fig. 6C). Trace amounts of molybdenite and other Cu sulfides, such as anilite, djurleite, geerite, spionkopite, and yarrowite, are found with S5 Dg and Bn (Yang et al. 2014; Wang et al. 2018). Rare S5 Ccp is intergrown with S5 Bn (Figs. 5G and H). Selenide and telluride form inclusions in stage 5 Bn and Ccp (Figs. 6D and E), in contrast to stages 1 and 2 Ccp and Bn.

Stage 5 chalcopyrite, bornite, and digenite are commonly replaced by stage 6 enargite-tennantite±tetrahedrite (Figs. 5F, G, and H). Stage 6 enargite (S6 Eng) and tennantite (S6 Tnt) characterize epithermal mineralization at shallow depths of 150–500 m in the alunite and kaolinite-dickite alteration zones, and they are hosted mostly by alunite-pyrite and kaolinite±pyrite veins (Figs. 2, 3, and 4). Less commonly, S6 Eng and Tnt replace stages 1 and 2 Ccp and Bn (Figs. 5I and J) in the D and A veins in the muscovite alteration zone (Fig. 4). Clausthalite inclusions are found in S6 Eng (Fig. 6F). Stage 6 tennantite replaces the porphyry stage chalcopyrite, bornite, and covellite (Fig. 5J) in the deep muscovite zone, where it is defined as deep tennantite (S6 Tnt-d), relative to the shallow tennantite (S6 Tnt-s) hosted in alunite and kaolinite veins, replacing S4 Py and S5 chalcopyrite-bornite-digenite (Fig. 5F and H). Stage 6 Tnt-d contains clausthalite inclusions (Fig. 6G). Stage 6 Tnt-s is commonly intergrown with enargite, and minor colusite (Fig. 5H and K), and it contains inclusions of galena, altaite, melonite, chalcopyrite, and native gold (Fig. 6D, H, and I). Tetrahedrite is found in small amounts in the periphery of the Tiegelongnan deposit with S6 Tnt-s. Rare sphalerite and galena occur in distal alunite veins, replacing chalcopyrite (Fig. 5L).

Supergene sulfides, mainly covellite (Cv-s), digenite (Dg-s), and chalcocite, are found beneath the supergene oxidation zone, overprinting parts of the alunite, kaolinite-dickite, muscovite, and chlorite alteration zones. Dg-s is characterized by the replacement of bornite with Cv-s (Fig. 5H). Supergene covellite is characterized by an association with goethite (Fig. 5C), and by replacement of chalcopyrite and bornite along their fractures or rims (Fig. 5H), in contrast to hypogene covellite that forms across the center of chalcopyrite and bornite grains (Fig. 5B and C). Supergene digenite and chalcocite occur at shallow depths and at the periphery of the deposit (Fig. 4).

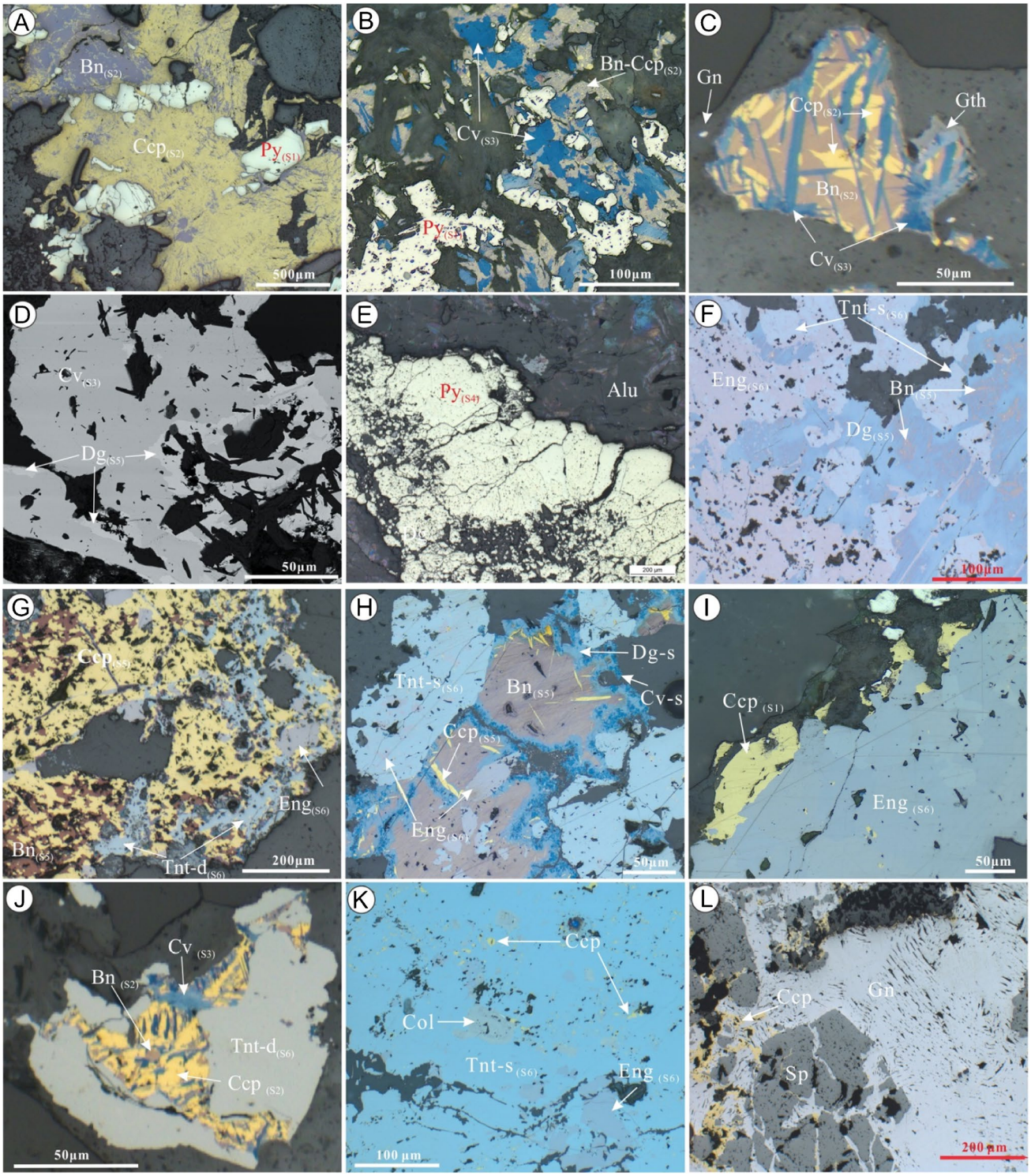

Sulfide geochemistry

EPMA results

Major elements (Cu, S, ± Fe,) in chalcopyrite, bornite, covellite, and digenite, and S and Fe in pyrite show narrow concentration ranges close to stoichiometric values (ESM 1 Table S1). Several covellite analyses from sample 4012-989 have high Fe contents ranging from 1.42 to 4.77 wt%. Pyrite contains several high Cu contents up to 2.43 wt%. Enargite has narrow S contents between 30.5 and 32.7 wt%, variable Cu concentrations between 45.2 and 50.8

◂**Fig. 5** Sulfide mineralogy paragenesis and intergrowth textures. **A** Chalcopyrite-bornite (S2) solid solution cementing fractured pyrite (S1), 2404-903. **B** Pyrite (S1) replaced by chalcopyrite and bornite (S2), which are then replaced by covellite (S3), 2404-712. **C** Chalcopyrite-bornite (S2) solid solution replaced by covellite (S3), and rimmed by goethite, 4012-989. **D** Covellite (S3) replaced by digenite (S5, BSE photomicrography), 2404-378. **E** Euhedral pyrite (S4) in alunite vein, 0804-408. **F** Bornite-digenite (S5) replaced by enargite, and tennantite (S6), 4004-447. **G** Chalcopyrite-bornite (S5) replaced by enargite and tennantite (S6), 2404-456. **H** Bornite, with chalcopyrite exsolution (S5), replaced by supergene digenite and covellite, and by tennantite and enargite (S6), 1604-149. **I** Enargite (S6) replacing chalcopyrite (S1) in quartz vein, 2404-883. **J** Tennantite (S6) replacing chalcopyrite-bornite (S2), and covellite (S3), 4012-989. **K** Enargite, colusite, and chalcopyrite inclusions in tennantite (S6), 1620-354. **L** Chalcopyrite and sphalerite, replaced by galena, 4012-354. Bn-bornite, Ccp-chalcopyrite, Col-colusite, Cv(-s)-covellite (supergene), Dg(-s)-digenite (supergene), Eng-enargite, Gn-galena, Py-pyrite, Sp-sphalerite, Tnt-d-tennantite in deep quartz veins, Tnt-s-tennantite in alunite and kaolinite veins. Reflected light microscope images, except for D

wt %, and As mostly ranges from 16.6 to 19.5 wt%. One enargite analysis (1620-354 Eng3) has a low As of 8.6 wt%, with a high Sn concentration of 6.8 wt% (ESM 1 Table S1). Iron in enargite varies from 0.66 to 2.55 wt%, with several data below the detection limit of 0.05 wt %. Tennantite contains narrow S and As ranges averaging 27.3 and 19.9 wt%, respectively, and a wide Cu concentration range from 42.0 to 53.8 wt%, with most data over the stoichiometric value of 10 atoms per formula unit (apfu; ESM 1 Table S1). Tennantite in sample 4012-989 Tnt2 has a low As of 17.4 wt%, and high Sb content of 3.8 wt% (ESM 1 Table S1). Cobalt and Zn contents of chalcopyrite, bornite, digenite, covellite, pyrite, and enargite are mostly below the EPMA detection limit of 0.03 wt% and 0.13 wt%, with the exception of one chalcopyrite Co data, and a few Zn analyses with values slightly above the detection limit (ESM 1 Table S1). Tennantite Co contents are between 0.03 and 0.33 wt%, and Zn is from 0.14 to 7.54 wt% (ESM 1 Table S1). Arsenic, Sn, and Sb in chalcopyrite, bornite, digenite, covellite, and pyrite are below 0.10 wt%, and some data are below the detection limit. Relatively high average Sb concentrations of 0.2 wt% in enargite and 0.3 wt% in tennantite were obtained. Lead concentrations are mostly higher than the detection limit of 0.04 wt%, with the exception of several bornite and digenite Pb data below the detection limit (ESM 1 Table S1). Tennantite has high Pb content of up to 2.49 wt%. Stage 6 Tnt-d and Tnt-s have distinct Cu, Fe, Zn, and Pb contents (ESM 1 Table S1). Stage 6 Tnt-d has lower Cu and Pb contents, with $mean_{Cu} = 45.8$ wt% and $mean_{Pb} = 0.3$ wt%, than that of Tnt-s with $mean_{Cu} = 50.6$ wt% and $mean_{Pb} = 0.8$ wt%. In contrast, S6 Tnt-d yields average Fe and Zn content of 2.1 wt% and 3.8 wt%, respectively, which are higher than S6 Tnt-s with Fe = 1.9 wt% and Zn = 0.3 wt%.

LA-ICP-MS trace element compositions

Porphyry mineralization sulfides, pyrite, chalcopyrite (S1 Ccp + S2 Ccp), bornite, and covellite have trace element concentrations mostly between 0.01 and 100 ppm (Fig. 7A and ESM 1 Table S3), with the exception of As, Se, and Pb in chalcopyrite, and Pb in bornite, that have median values between 100 and 1000 ppm (Fig. 7A). Palladium concentrations in those sulfides are low, with the majority of values less than 0.01 ppm. Among the porphyry stage Cu-sulfides, chalcopyrite has the highest median values of V, Co, As, Mo, Ag, In, Sb, Au, Tl, and Pb, whereas covellite has the highest contents of Bi, Se, Sn, Te, and W (Fig. 7A). Bornite contains the lowest concentrations of As, Co, Ga, Mn, Ni, Se, Sn, Te, V, and W. Pyrite has significantly lower Ag, Au, Cd, Ga, In, Mo, Pb, Tl, and Zn contents, but higher Co and Ni contents than the Cu-sulfides (Fig. 7A). Most trace elements in chalcopyrite are hosted as solid solutions, evidenced by stable LA-ICP-MS signal spectra, with the exception of the irregular spectra of Zn and Te, which suggest a heterogeneous distribution (ESM 2 Fig. S1A). Sphalerite inclusions are likely to present in bornite, causing abrupt Zn spikes of LA-ICP-MS spectra (ESM 2 Fig. S1C). Most trace elements in covellite are heterogeneous, as shown by spiky laser spectra (ESM 2 Fig. S1D).

Epithermal chalcopyrite, bornite, digenite, enargite, tennantite, and pyrite contain variable contents of several elements (Fig. 7B). Most of the element concentrations in chalcopyrite are low, with only Se having a median value over 100 ppm. Chalcopyrite contains the highest median value of In. Abrupt As, Co, Zn, Sb, and V counts in chalcopyrite (ESM 2 Fig. S1B) may result from inclusions of other minerals. Bornite has median concentrations of most trace elements less than 10 ppm, but that of Pb is over 100 ppm, with the lowest contents of several elements such as Au, Cd, Co, In, Mo, Sb, Te, V, W, and Zn, compared to other epithermal Cu-sulfides (Fig. 7B). Digenite contains median concentrations of all elements less than 100 ppm, with the lowest Pd contents relative to other Cu-sulfides (Fig. 7B). The unstable laser signals of digenite (ESM2 Fig. S1E) suggest the heterogeneity of several trace elements. Enargite and tennantite have elevated concentrations of Bi, Cd, Sb, Sn, Te, and Zn, with Sb up to thousands of ppm (Fig. 7B). Lead is heterogeneous in enargite, as shown by its spiky laser signal (ESM 2 Fig. S1F and G). Tennantite incorporates the highest median concentrations of many trace elements, including Ag, Au, Bi, Cd, Co, Hg, Ni, Pb, Pd, Sn, Sb, Te, Tl, W, and Zn relative to other epithermal sulfides (Fig. 7B). Gold inclusions in tennantite are shown by spiky laser counts (ESM 2 Fig. S1H), but gold mainly occurs in solid solution, as shown

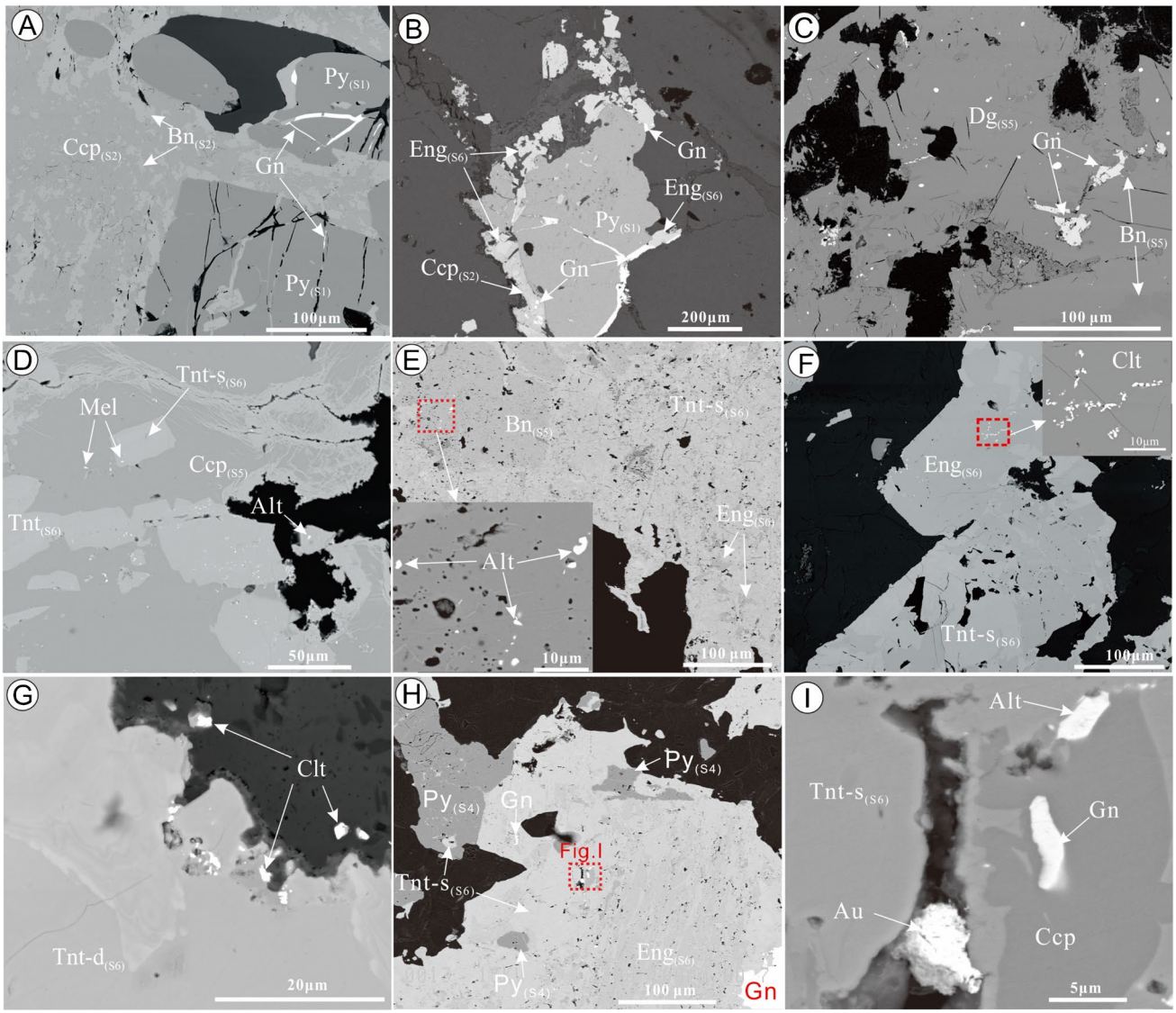

Fig. 6 BSE photomicrograph showing mineral textures and inclusions in Cu-sulfides. **A** Pyrite (S1) surrounded by chalcopyrite and bornite (S2) with galena veins, 2404-903. **B** Pyrite (S1) surrounded by enargite (S6) and chalcopyrite (S2) with galena inclusions, 1604-650. **C** Galena inclusions in digenite and bornite (S5), 2404-374. **D** Chalcopyrite (S5) with melonite (Mel) replaced by tennantite (S6) with melonite (Mel) and altaite (Alt) inclusions, 1620-354. **E** Bornite (S5) with altaite (Alt) inclusions replaced by enargite and tennantite (S6), 1604-149. **F** Enargite with clausthalite (Clt) inclusions replaced by tennantite (S6), 1604-409. **G** Tennantite in deep quartz veins (S6 Tnt-d) with banding, hosting clausthalite (Clt) inclusions, 4012-989. **H** Intergrown enargite and tennantite in alunite veins (S6 Tnt6-s) replacing stage 4 pyrite, 1604-231. **I** Native gold, galena, chalcopyrite, and altaite inclusions in tennantite (S6), 1604-231. Abbreviations as in Fig. 5

by its flat laser signal (ESM 2 Fig. S1I). Heterogeneity of Sb, Pb, and Ag in tennantite is shown by irregular laser signals (ESM 2 Fig. S1I). Epithermal pyrite shows large trace element concentration ranges, with the highest median value of Ni relative to other epithermal sulfides (Fig. 7B).

In terms of the different stages of chalcopyrite, S1 Ccp has the highest contents of Mn, Ni, Se, and Sn; and S2 Ccp contains the highest concentrations of Ag, Au, Ga, Mo, Pb, Te, Tl, and V, whereas the S5 Ccp contains the most As, Co, and In (ESM 2 Fig. S2A). For bornite, S2 Bn contains higher contents of Ag, Au, In, Mo, Se, Tl, and V, and lower contents of As, Bi, Co, Ga, Mn, Ni, Pb, Pd, Sn, and Te, compared to S5 Bn (ESM 2 Fig. S2B). The LA-ICP-MS mapping of coexisting S2 Ccp and Bn show that V, Mo, In, Sb, Au, Tl, and Pb are enriched in S2 Ccp (ESM 2 Fig. S3), but Bi is concentrated in S2 Bn. Stage 6 Tnt-d contains higher concentrations of V, Co, Ni, Zn, Pd, Cd, In, Sn, and Tl, but lower Mn, Ga, Mo, Au, Hg, and Bi than S6 Tnt-s (ESM 2 Fig. S2C). Concentrations of Se, Ag, Sb, Te, and Pb are close in both groups of tennantite (ESM 2 Fig. S2C). Stage

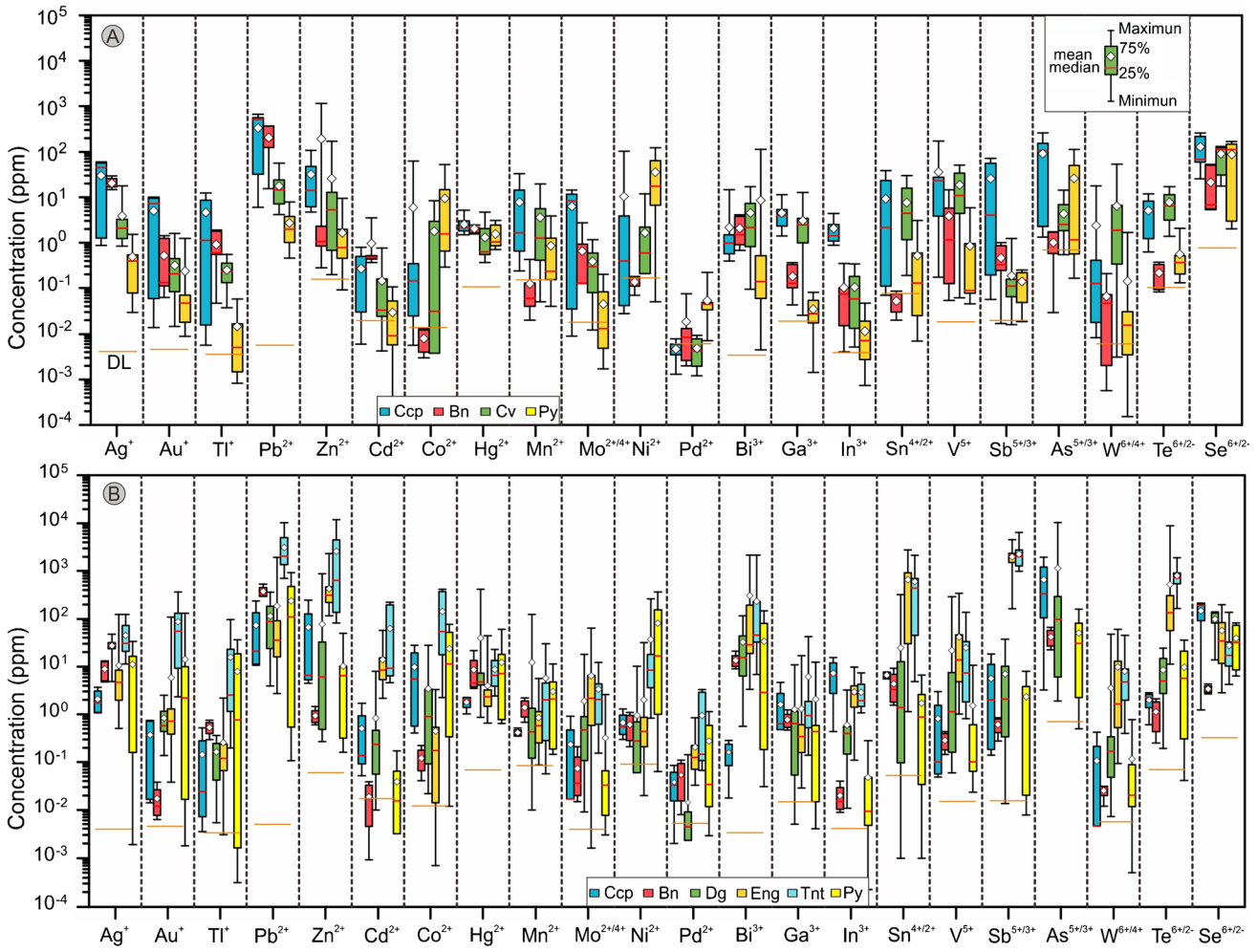

Fig. 7 Trace element concentration of sulfides in the Tiegelongnan deposit. Porphyry stage Cu-sulfides (**A**) and epithermal stage Cu-sulfides (**B**). Abbreviations as in Fig. 5

4 Py contains large concentration ranges of trace elements, with most median values higher than S1 Py, excluding Se and Pd (ESM 2 Fig. S2D).

Multivariate statistical analysis

PLS-DA results of porphyry sulfides indicate that chalcopyrite has negative qw^*_2 and slightly positive qw^*_1 loadings, associated with Ga, In, Sb, Au, and Zn (Fig. 8A), and plots with negative t_2 scores (Fig. 8B). Lead and Mo also have positive score contributions to chalcopyrite (ESM 2 Fig. S4A). Bornite plots with positive loadings of qw^*_1 and qw^*_2 due to correlations with Ag, Cd, Hg, Tl, Mo, and Pb (Fig. 8A), with positive scores of t_1 and t_2 (Fig. 8B). Score contribution plots of bornite show that Au, Sb, and Bi also contribute positively to discriminating bornite from chalcopyrite and covellite (ESM 2 Fig. S4B). Covellite plots with negative loading of qw^*_1 and slightly positive qw^*_2 correlated with Te, W, Bi, Se, V, Co, Ga, and Sn (Fig. 8B), consistent with positive score contributions of these elements for covellite (ESM 2 Fig. S4C).

PLS-DA plots of epithermal sulfides indicate that chalcopyrite data plot close to origin loading (Fig. 8C), such that it is not well discriminated by PLS-DA. Bornite has high qw^*_1 and slightly negative qw^*_2 loadings due to correlations with Co, Tl, Pb, Ga, Hg, Ag, Se, and Bi (Fig. 8C), which yields positive t_1 scores (Fig. 8D). Gallium, Ag, Hg, Tl, and Pb have positive score contributions to bornite (ESM 2 Fig. S3E). Digenite plots in positive qw^*_1 and qw^*_2 quadrants due to correlations with Ga, Ag, Hg, and Se (Fig. 8C), with positive scores of t_1 and t_2 (Fig. 8D). The score contribution plot indicates that V, Co, Mo, Au, Tl, Pb, and Bi are positive in digenite (ESM 2 Fig. S4F). Enargite plots with negative qw^*_1 and positive qw^*_2 loadings, correlated to Sb, Cd, Zn, Te, W, V, Mo, Sn, and In (Fig. 8C). The score contributions plot of enargite (ESM 2 Fig. S4G) shows that Bi is another element to discriminate enargite from other epithermal sulfides. Tennantite plots with negative qw^*_2 loadings

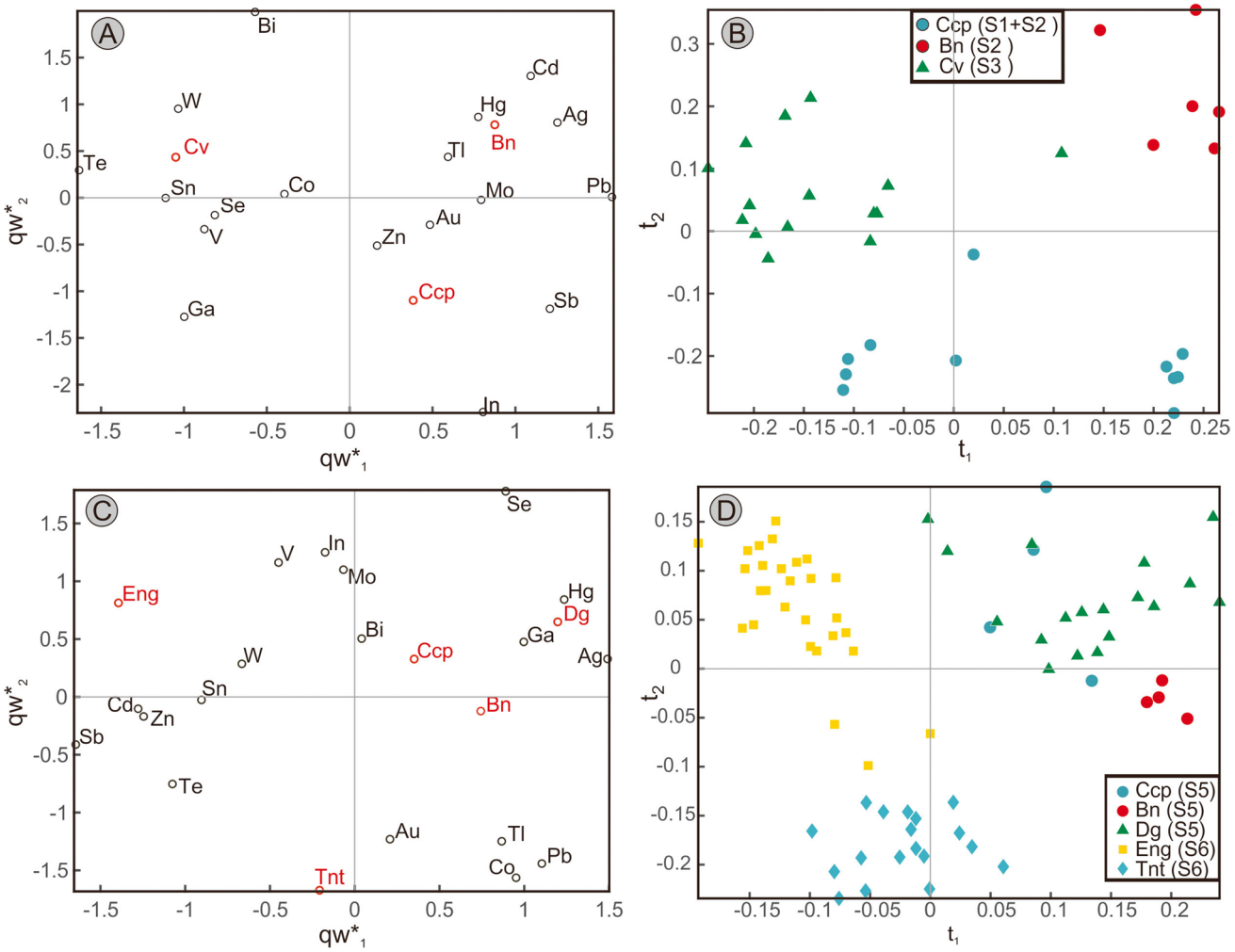

Fig. 8 PLS-DA results of Cu-sulfides LA-ICP-MS trace element geochemistry. **A** Loadings biplots $qw*_1$-$qw*_2$ (first and second loadings) of porphyry Cu-sulfides. **B** Scores scatter plot t_1-t_2 (first and second scores) for porphyry Cu-sulfides. **C** Loadings biplots $qw*_1$-$qw*_2$ of epithermal Cu-sulfides. **D** Scores scatter plot t_1-t_2 for epithermal Cu sulfides. In biplots $qw*_1$-$qw*_2$, elements plotting in the vicinity of each other show strong positive correlations, whereas those negatively correlated are in the opposite quadrant. Abbreviations as in Fig. 5

for the correlations with Au, Co, Tl, Pb, Te, Sb, Zn, Sn, and Cd (Fig. 8C), with negative t_1 scores (Fig. 8D), consistent with the positive score contributions of those elements for tennantite (ESM 2 Fig. S4H).

Discussion

Trace element substitution in sulfides

The enargite and tennantite have significantly high contents of Zn, Cd, Pb, Sn, Sb, Bi, and Te, relative to other sulfides. Antimony and Sn in enargite and tennantite can substitute with As, as shown by EPMA data for enargite (1620-354 Eng3) with high Sn, and tennantite analyses (2404-989 Tnt2) with high Sb contents, but both with low As contents (ESM 1 Table S1). High Sb concentrations in enargite and tennantite have also been found in other studies, where they were interpreted to result from Sb substitution for As (Maske and Skinner 1971; Posfai and Buseck 1998; Deyell and Hedenquist 2011; George et al. 2017). On the other hand, As may favor incorporating other trace elements, by substituting for Cu, and contribute to higher concentrations of Bi, Cd, Sb, Sn, Te, Zn, and Pb in these two minerals relative to other sulfides (Fig. 7B). The substitution of Cu by another metal is complex because of ionic charge and radii balance with the replaced Cu^+ in Cu-sulfides (Goh et al. 2006; Pearce et al. 2006; Xie et al. 2013). For example, some monovalent ions, such as Ag^+, Au^+, and Tl^+, have larger ionic radii than Cu^+, whereas other ions with similar radii to Cu^+, such as Zn^{2+}, Sb^{3+}, In^{3+}, and Sn^{4+}, have higher ionic charges. As^{5+} and As^{3+} in enargite and tennantite are high charge ions,

which could be coupled with Cu^+ to maintain ionic charge balance during the substitution of monovalent, divalent, trivalent, and tetravalent ions. Liu et al. (2019) proposed substitution of $As^{5+} + Cu^+$ in enargite as reaction of (Ag, Au, and/or Tl)$^+$ + (Fe, Cd, Zn, and/or Pb)$^{2+}$ + (Sn, Te, and/or Ge)$^{4+} \leftrightarrow As^{5+} + 2Cu^+$. He et al. (2018) found a high content of Ag, up to 10 wt% in tetrahedrite at Tiegelongnan, which may result from the coupled incorporation with As.

Additionally, As has been shown to play a significant role in the coupled incorporation of Au and Ag in other sulfides, such as pyrite and digenite (Reich et al. 2005; Deditius et al. 2009; Large et al. 2009; Wu et al. 2019b), Reich et al. (2010) suggested that high contents of Au and Ag in digenite resulted from the reaction $As^{3+} + 3(Au^+/Ag^+) = 4Cu^+$. In this study, Au and Ag in chalcopyrite and enargite show a positive correlation (Fig. 9A), suggesting a similar substitution behavior of Ag and Au, both common monovalent and large radii cations. A positive correlation between As and Au is shown in chalcopyrite and covellite (Fig. 9B). It suggests that the incorporation of Au in chalcopyrite and covellite is related to As, which may also apply to other Cu-sulfides.

Positive correlations between Au and Te are shown for chalcopyrite and covellite (Fig. 9C). Chouinard et al. (2005) suggested that Te causes lattice expansion of pyrite, and provides space for the large Au ion by substituting for S^{2-}. Therefore, the incorporation of Au in Cu-sulfides can be described by the reaction $As^{3+} + (Au^+/Ag^+) + Te^{2-} \leftrightarrow 4Cu^+ + S^{2-}$.

Chalcopyrite and bornite have an extra Fe site to hold trace elements, compared to covellite and digenite. Incorporation of elements by substitution for Fe^{2+} in chalcopyrite might be one reason why porphyry stage chalcopyrite has higher contents of several elements compared to covellite, particularly the divalent metals, such as Pb, Zn, Cd, Co, Hg, Mn, Mo, and Ni (Fig. 7A), and porphyry S2 Bn also has some divalent element Pb, Cd, Hg, Mo, and Pd contents higher than covellite.

Bornite has lower concentrations of several elements compared to covellite and chalcopyrite (Fig. 7), likely due to trace element partitioning between chalcopyrite and bornite. In stage 2 sulfides, the average concentrations of most elements are higher in chalcopyrite than the coexisting bornite, with the exception of Pd, Cd, and Zn (ESM 1 Table S3). LA-ICP-MS maps of coexisting S2 Ccp and Bn also indicate that V, Mo, In, Sb, Au, Tl, and Pb are enriched in S2 Ccp, whereas Bi is enriched in S2 Bn (ESM 2 Fig. S3).

Several trace elements in S5 Ccp and Bn show similar partitioning trends, compared to S2 Ccp and Bn, wherein median contents of Co, Sb, Te, Ga, W, Au, Mo, V, In, Sn, and Se are higher in S5 Ccp, and Pd is higher in S5 Bn (ESM 1 Table S3). There is a general trend that Co, Sb, Te, Ga, W, Au, Mo, V, In, Sn, and Se are partitioning in chalcopyrite, whereas Bi and Pd are favored in bornite.

Control from hydrothermal physicochemical environments

The evolution of sulfides in magmatic-hydrothermal systems is interpreted with regard to the sulfidation state, which is an integrated function of fS_2, temperature, hydrothermal fO_2, and pH conditions (Einaudi et al. 2003). Porphyry Cu-sulfides evolve from S1 chalcopyrite-pyrite ± molybdenite, to S2 chalcopyrite-bornite, and finally to S3 covellite in the Tiegelongnan deposit, suggesting an evolution path from intermediate to high and then very high sulfidation states (Fig. 10). According to the PLS-DA results, the trace element composition evolves with the sulfidation state, from enrichment in Au, Zn, Mo, Pb, In, Sb, and Ga in chalcopyrite, to Ag, Au, Tl, Cd, Mo, Hg, Pb, Bi, and Sb in bornite, and Co, Ga, Bi, Sn, V, Te, W, and Se enrichment in S3 Cv (Fig. 10). Epithermal Cu-sulfides evolve from S5 digenite-bornite-chalcopyrite to S6 enargite-tennantite, along a decreasing sulfidation state path (Fig. 10). The occurrence of chalcopyrite with tennantite (Figs. 5K and 6I) indicates the epithermal tennantite formed at an intermediate sulfidation state (Einaudi et al. 2003). The PLS-DA results (Fig. 8) suggest that high sulfidation state S5 Bn is associated with enrichment of Ag, Tl, Pb, Co, Hg, Ga, and Se, and S5

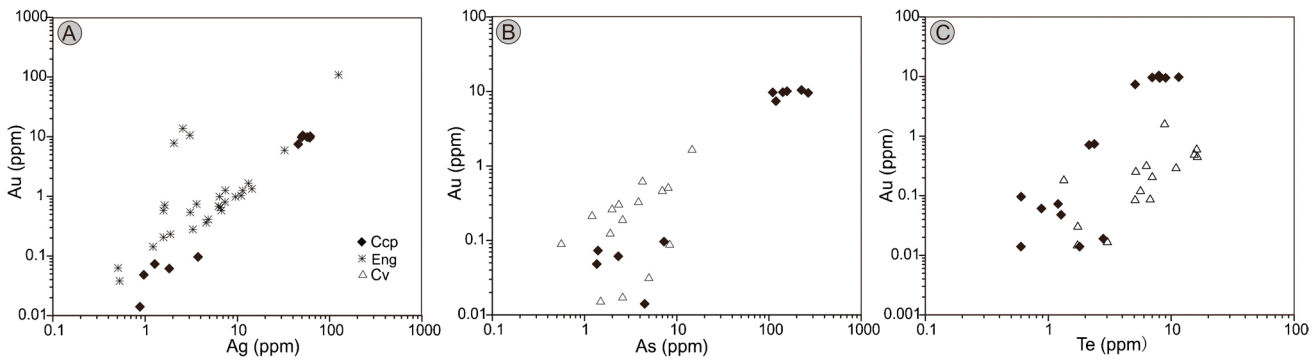

Fig. 9 Correlationship between Ag and Au (**A**), As and Au (**B**), Te and Au (**C**)

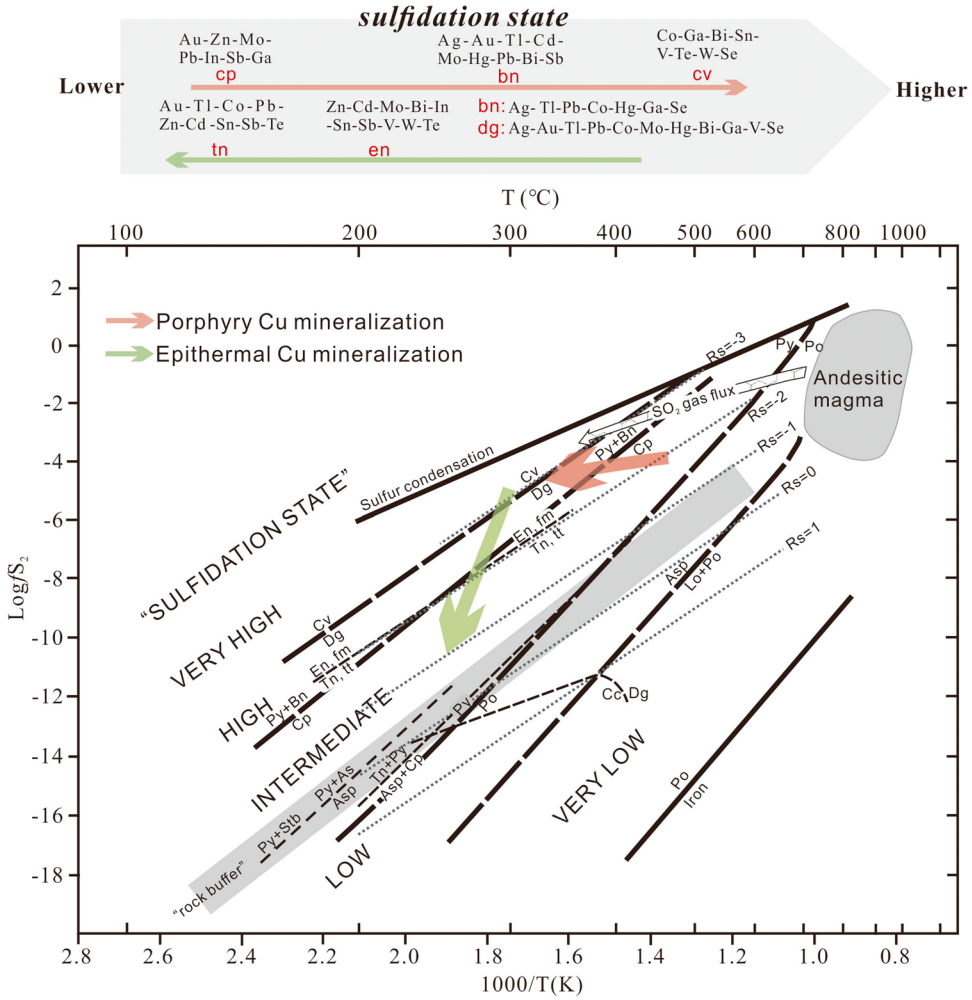

Fig. 10 Evolution of sulfidation state and associated trace elements during porphyry and epithermal mineralizations at Tiegelongnan, modified after Einaudi et al. (2003). Porphyry mineralization sulfides evolve from intermediate (stage 1 chalcopyrite), to high (stage 2 bornite), and very high sulfidation state (stage 3 covellite); Epithermal mineralization sulfides evolve from high (stage 5 bornite-digenite) to intermediate sulfidation state (stage 6 tennantite). Asp-arsenopyrite, Bn-bornite, Cc-chalcocite, Cv-covellite, Cp-chalcopyrite, Dg-digenite, En-enargite, Fm-famatinite, Py-pyrite, Po-pyrrhotite, Stb-stibnite, Tn-tennantite, Tt-tetrahedrite

Dg rich in Ag, Au, Tl, Pb, Co, Mo, Hg, Bi, Ga, V, and Se (Fig. 10). Stage 6 Eng has high Zn, Cd, Mo, Bi, In, Sn, Sb, V, W, and Te, whereas S6 Tnt is characterized by high Au, Tl, Co, Pb, Zn, Cd, Sn, Sb, and Te (Fig. 10).

The enrichment of elements in epithermal enargite and tennantite, such as As, Te, Sb, Ag, Au, Pb, and Zn, partition into aqueous vapor as hydroxide complexes, during ascent into shallow epithermal environments (Pokrovski et al. 2002, 2005; Simmons et al. 2016). In addition, epithermal mineralization stage S5 Ccp and Bn both have higher contents of As and Pd than porphyry stage chalcopyrite (S1 and S2 Ccp) and S2 Bn (ESM 2 Fig. S2 A and B). Although Pd concentrations in the hydrothermal fluids are unknown, As is believed to be abundant in epithermal fluids (Pokrovski et al. 2002, 2005; Simmons et al. 2016). However, Rottier et al. (2018) argued that there is no connection between sulfide and hydrothermal fluid compositions at the Cerro de Pasco epithermal deposit, Peru. On the other hand, partitioning of As and Pd to chalcopyrite and bornite is likely higher at the lower temperatures of epithermal mineralization than that of porphyry mineralization at Tiegelongnan. At the Lihir gold deposit, Sykora et al. (2018) found that low-temperature epithermal stage pyrite had higher Ag, Au, Mo, As, and Sb contents than high-temperature porphyry stage pyrite. Our results are consistent with this, with epithermal S4 Py having higher concentrations of most elements than porphyry S1 Py, with the exception of Se and W (ESM 2 Fig. S2D).

In contrast, the Au concentrations in coexisting stages 2 and 5 chalcopyrite and bornite at Tiegelongnan show a decreasing trend with lower temperatures. Stage 2 chalcopyrite and bornite formed at temperatures of ~ 350 ℃, based on fluid inclusion studies (Yang et al. 2014; He et al. 2017), whereas epithermal S5 chalcopyrite and bornite formed at ~ 250 ℃, based on stable isotope equilibrium temperatures (Yang et al. 2020a). The Au concentrations follow the decreasing trend of coexisting bornite and chalcopyrite Au concentrations at temperatures from 600 and 400 ℃ (Fig. 11A; Simon et al. 2000). However, chalcopyrite is a dominant Au carrier at Tiegelongnan, with higher Au (median = 9.7 ppm) in S2 Ccp than in S2 Bn (median = 0.1 ppm), and higher Au (median = 0.4 ppm) in S5 Ccp than S5 Bn (median = 0.01 ppm; Fig. 11C). This

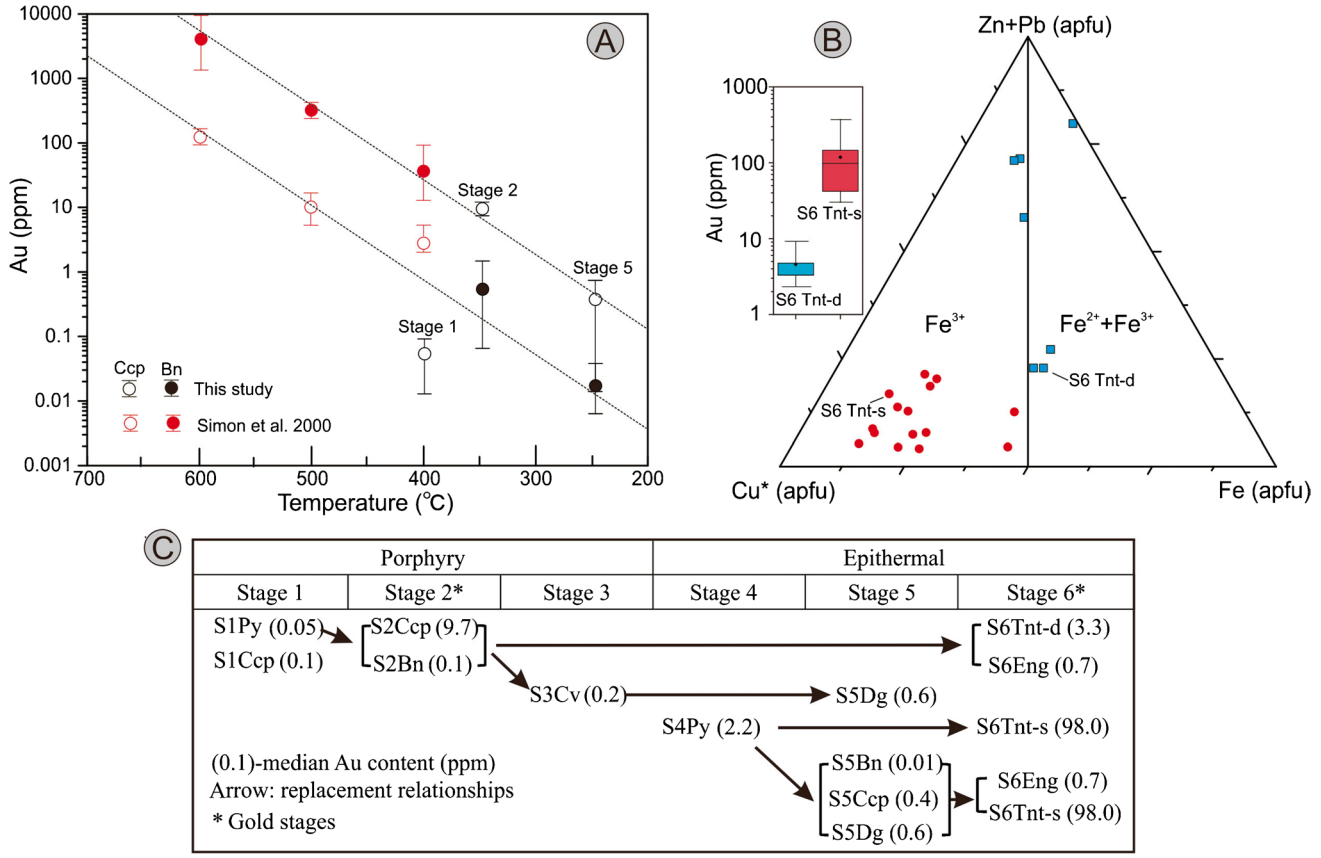

Fig. 11 Relationship between gold content and hydrothermal factors. **A** Chalcopyrite and bornite Au correlation to temperature, modified after Simon et al. (2000). **B** Tennantite oxidation condition and Au correlation, ternary diagram modified after Catchpole et al. (2012). **C** Gold median values for each stage of sulfides, and their replacement relationship. Cu*, excess Cu over 10 apfu. Abbreviations as in Fig. 5

is distinct from the close spatial Au-bornite correlation observed in several other porphyry deposits (e.g., Bingham deposit, USA; Redmond and Einaudi 2010), and the experimental data of Simon et al. (2000), where bornite is the predominant Au carrier at high temperatures (Fig. 11A). The close correlation between bornite and gold at Bingham, which formed at temperatures of 425–350 ℃ (Redmond et al. 2004; Landtwing et al. 2005), is higher than the mineralization temperatures (~350 and ~250 ℃) in the Tiegelongnan deposit. Therefore, a lower temperature (< 350 ℃) perhaps explains the partitioning of Au in chalcopyrite relative to bornite at Tiegelongnan.

However, a lower temperature cannot explain higher Au content (median = 9.7 ppm) in S2 Ccp formed at ~ 350 °C (He et al. 2017), compared to low Au content (median = 0.1 ppm) of S1 Ccp, formed at around ~ 400 °C (Fig. 11A, C; Yang et al. 2014). Sulfur isotopes indicate that hydrothermal fluids evolved from S1 sulfides with average $\delta^{34}S_{H2S} = -2.5‰$ to S2 sulfides with average $\delta^{34}S_{H2S} = -5.6‰$ (Yang et al. 2020a). The S isotope composition of hydrothermal fluids is determined by temperature and redox state, assuming that the bulk S isotopic composition is constant in the porphyry system (Rye and Ohmoto 1974; Rye 1993). The declining temperature from ~ 400 °C for S1 sulfides to ~ 350 °C for stage 2 sulfides yields an increase in S isotopic fractionation between aqueous SO_4^{2-} and H_2S of 2.4‰, from 14.5 to 16.9 ‰ (Eldridge et al. 2016). This change in temperature-driven fractionation of 2.4‰ is smaller than the change in fluid $\delta^{34}S_{H2S}$ of 3.1‰, suggesting that the temperature decrease was accompanied by an increase in the oxidation state of the fluids from S1 to S2. The higher gold content of S2 chalcopyrite (median = 9.7 ppm Au), compared to S1 Ccp (median = 0.1 ppm Au; Fig. 11C), suggests that high gold in chalcopyrite may be controlled by a higher hydrothermal oxidation state under decreasing temperature.

The high oxidation state is also likely one of the reasons for a higher content of Au in S6 Tnt-s (median = 98.0 ppm), than in S6 Tnt-d (median = 3.3 ppm; Fig. 11C and ESM 2 Fig. 2C). Most S6 Tnt-d and Tnt-s in the Tiegelongnan deposit display Cu-excess, which is defined by more than 10 apfu Cu (ESM 1 Table S1; Marcoux et al. 1994). The excess Cu (> 10 apfu Cu), Pb–Zn, and Fe contents are related to the redox state of hydrothermal fluids (Charlat and Levy 1974; Catchpole et al. 2012). The ternary diagram indicates that S6

Tnt-s plots near the Fe^{3+} pole at more oxidizing conditions, having two orders of magnitude higher Au contents than S6 Tnt-d, which plots in the transition zone between Fe^{3+} and $Fe^{2+} + Fe^{3+}$ (Fig. 11B).

The high redox state is an essential factor for high Au solubility in hydrothermal fluids. Because Au is dominantly transported by S-bearing complexes, whose behavior is sensitive to redox state, they deposit as sulfides under reduced H_2S-saturated environments (Seward 1973; Heinrich et al. 2004; Seo et al. 2009). Alternatively, a high oxidation state in hydrothermal fluids can change the Cu valency, increasing the solubility of Au and other elements in sulfides. For example, Chouinard et al. (2005) and Pacevski et al. (2008) suggested that a high redox state oxidizes Cu^+ to Cu^{2+}, which directly substitutes for Fe^{2+} in pyrite, and accounts for the distortion of the pyrite lattice and incorporation of high concentrations of other trace elements, including Au. The Cu-excess tennantite reflects an oxidizing environment, under which Cu^+ can be oxidized to Cu^{2+} when tennantite contains more than 11 apfu of Cu (Catchpole et al. 2012). The S6 Tnt-s has more than 11 apfu Cu excess (ESM 1 Table S1), suggesting the presence of Cu^{2+}, which likely increased the solubility of Au in S6 Tnt-s.

Remobilization of metals during sulfide replacement

Gold remobilization during the replacement of sulfides is common (Large et al. 2009, 2012; Deditius et al. 2014; Wu et al. 2019a). At Tiegelongnan, porphyry S1 Py (with Au median = 0.05 ppm) is replaced by S2 Ccp (Au median = 9.7 ppm) and S2 Bn (Au median = 0.1 ppm; Fig. 11C). Thus, the Au content in S1 Py is too low to account for higher Au contents in S2 Ccp. Instead, the higher oxidation state during S2 likely introduced gold into the Tiegelongnan porphyry system with preferential partitioning of gold in S2 Ccp over Bn. Porphyry S2 Ccp and Bn are locally replaced by epithermal S6 Eng (Au median = 0.7 ppm) and Tnt-d (Au median = 3.3 ppm; Fig. 11C) at depth, suggesting that gold in S6 Eng and Tnt-d was likely partly leached from S2 Ccp. However, S6 Eng and Tnt-d have low gold contents, thus the contribution to epithermal Au mineralization was likely minor.

Epithermal S4 Py, has a large gold concentration range (SEM 2 Fig, S3D), with a median value of 2.2 ppm (Fig. 11C). The S4 pyrite sample 1604-231, which has been replaced by S6 Tnt-s (Fig. 6H) with a high Au content of median = 98.0 ppm (Fig. 11C), has a low Au content (median = 1.7 ppm), whereas sample 0804-408, which has not been replaced by tennantite (Fig. 5E), has a high Au content (median = 25.0 ppm; ESM 1 Table. S3). The gold from S4 Py was likely leached and incorporated by S6 Tnt-s, but the high content of gold in S6 Tnt-s would require a tenfold volume replacement which is not supported by petrographic evidence. The high gold content in S6 Tnt-s (median = 98.0 ppm), forming rims around S6 Eng (median = 0.7 ppm; Fig. 6F and H), suggests addition of new gold at the end of the paragenetic sequence of the Tiegelongnan deposit. Other sulfide replacements do not show remobilization and enrichment of gold to later sulfides (Fig. 11C). Therefore, the epithermal sulfide replacement reactions are unlikely to have leached significant gold from earlier sulfides at Tiegelongnan.

Several studies have shown that Cu from deep porphyry mineralization can be remobilized in high-grade phyllic (muscovite) alteration (Sillitoe 2010), and in shallow epithermal Cu mineralization, such as at Butte, USA (Brimhall 1980), Chuquicamata, Chile (Ossandón et al. 2001), and Alter, Argentina (Maydagán et al. 2015). Diamond drilling so far has not intersected a high-temperature potassic alteration zone at Tiegelongnan, except for drill-hole 4804 that intersected deep potassic (biotite) alteration that yielded a lower Cu grade (< 0.5 wt% Cu) than the upper muscovite alteration zone (Figs. 2B and 4). Thus, the Tiegelongnan deposit may have remobilized Cu from deep concealed potassic alteration. Epithermal sulfides replacing earlier porphyry stages 2 and 3 sulfides (Fig. 11C) correspond closely to several Cu enrichment zones (> 0.8 wt %) in the shallow epithermal system (Fig. 4), which indicates that Cu has been remobilized by the epithermal fluids.

Implication for exploration

The distribution of sulfides and associated trace elements at Tiegelongnan are shown in a schematic model in Fig. 12, based on the spatial distribution of sulfides (Fig. 4) and sulfide-element evolution (Fig. 10). At depth, in the zone of biotite and deep muscovite alteration, mineral assemblages evolve from chalcopyrite-pyrite-molybdenite to chalcopyrite-bornite towards lower elevations. The replacement of the muscovite alteration by the alunite-kaolinite alteration at intermediate depths is associated with precipitation of covellite, digenite, bornite, enargite, and tennantite. Enargite, tennantite, bornite, and digenite are the principal sulfides in the shallow, alunite-kaolinite alteration zone, and they also locally replace porphyry stage chalcopyrite, bornite, and covellite in the overprinting zone (Fig. 12). Minor amounts of sphalerite and galena are found at the periphery of the muscovite and alunite-kalinite alteration zones. The deep porphyry sulfides chalcopyrite-bornite-molybdenite, shallow epithermal high-sulfidation sulfide enargite-digenite-tennantite assemblages, and distal galena and sphalerite at Tiegelongnan are consistent with observations in many porphyry systems (Einaudi et al. 2003; Sillitoe 2010). Along with the spatial distribution of sulfides, there is a metal zonation pattern (Fig. 12). Porphyry S2 chalcopyrite at depth in

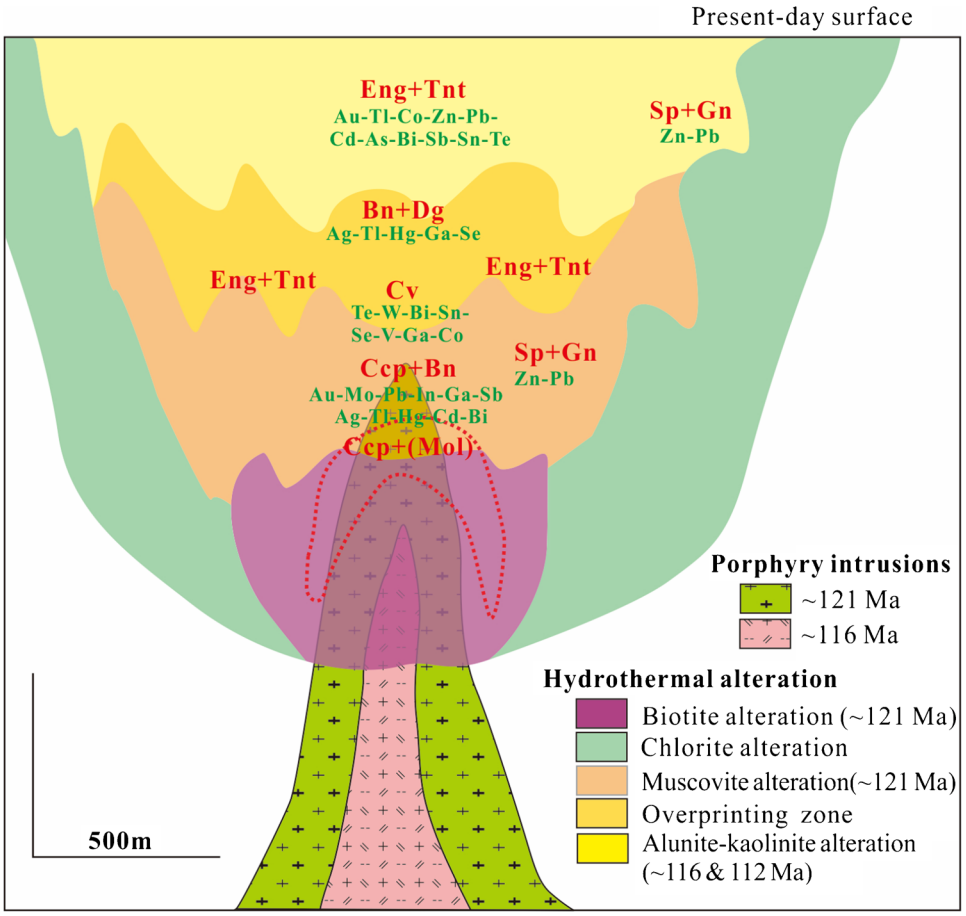

Fig. 12 Schematic model of alteration, sulfides, and metals distribution in the Tiegelongnan porphyry-epithermal system. Mol-molybdenite, Sp-sphalerite, other abbreviations as in Fig. 5. Geochronology from Yang et al. (2020b)

Tiegelongnan is associated with high Au, Mo, In, Ga, and Sb contents. Porphyry S2 bornite has high Ag, Hg, Tl, Cd, Bi, Au, Mo, and Sb. Covellite (S3 Cv) is characterized by high contents of Te, W, Bi, Sn, Se, V, Ga, and Co, whereas epithermal S5 bornite and digenite display high Ag, Tl, Hg, Ga, and Se contents. Stage 6 enargite and tennantite are associated with Au, Tl, Co, Cd, Bi, As, Sb, Sn, and Te.

The sulfide trace element spatial distribution pattern at Tiegelongnan is similar to metal spatial distribution in other porphyry Cu systems (Halley et al. 2015). Gold is commonly associated with porphyry chalcopyrite-bornite at depth and shallow epithermal enargite and tennantite in porphyry and epithermal deposits (Sillitoe 2010; Kouzmanov and Pokrovski 2012), which is consistent with the enrichment of Au in sulfides at Tiegelongnan. Halley et al. (2015) illustrated that high Mo, Bi, Se, and Te contents characterize the deep potassic alteration zone. In deep porphyry mineralization, high Mo contents mainly result from molybdenite (Kouzmanov and Pokrovski 2012), which occurs in the deep Tiegelongnan porphyry system. The Mo enrichment in chalcopyrite and bornite and high Bi content in bornite (Fig. 12) may also relate to high Mo and Bi at depth. High As, Sb, Bi, Te, W, and Se contents characterize sericite alteration zone, similar to typical high As, Sb, Tl, and Bi contents in the advanced argillic alteration (Halley et al. 2015). The similar enriched metals in the sericite and shallow advanced argillic alteration zones are consistent with similar sulfide assemblages, with high sulfidation state covellite, digenite, and enargite in sericite and advanced argillic alterations in several porphyry deposits (Sillitoe 2010). The Cu-sulfide trace elements—including Te, W, Bi, and Se in covellite; Se in bornite and digenite; and As, Sb, Tl, and Bi in enargite (Fig. 12)—correspond to the metals distribution of Halley et al. (2015), suggesting that sulfide distribution and their trace elements control metals' spatial distribution in the porphyry-epithermal systems. Therefore, the trace element-sulfide correlations and their distribution at Tiegelongnan (Fig. 12) can be potential for exploring porphyry systems overprinted by epithermal mineralization.

Conclusions

1. Sulfides formed during porphyry mineralization at Tiegelongnan evolve from stage 1 chalcopyrite-pyrite ± molybdenite, to stage 2 chalcopyrite-bornite, and to stage 3 covellite, along an increasing sulfidation path, whereas the sulfides of epithermal miner-

alization evolve from stage 4 pyrite-alunite, to stage 5 digenite-bornite-chalcopyrite, and to stage 6 enargite-tennantite ± tetrahedrite, suggesting a decreasing sulfidation trend.

2. Trace elements partitioning between coexisting chalcopyrite and bornite causes Au and other trace elements to become enriched in chalcopyrite formed at low temperatures (< 350 ℃). The low-temperature epithermal environment (~ 250 ℃) may cause partitioning of Au, Zn, Cd, Pb, As, Sn, Sb, Bi, and Te to enargite and tennantite, and As and Pd to epithermal chalcopyrite and bornite relative to porphyry ones.
3. Stage 2 chalcopyrite is the major porphyry Au host (median = 9.7 ppm), whereas stage 6 tennantite in the alunite veins (S6 Tnt-s Au median = 98.0 ppm) is the major epithermal Au host. The incorporation of Au in Cu-sulfides is related to the high oxidation state of the hydrothermal system. The incorporation of Au in Cu-sulfides likely resulted from the reaction of $As^{3+} + (Au^{+}/Ag^{+}) + Te^{2-} \leftrightarrow 4Cu^{+} + S^{2-}$.
4. Epithermal sulfide replacement may remobilize Cu from earlier porphyry mineralizations. Gold may not have been remobilized during the sulfide replacement.
5. The Cu-sulfides and related trace elements show a systematic spatial distribution. Chalcopyrite is the major Au, Mo, In, Sb, and Ga carrier in deep porphyry mineralization, whereas porphyry bornite is associated with Ag, Tl, Hg, Cd, and Bi at depth. Covellite incorporate Te, W, Bi, Ga, Sn, V, and Se, and epithermal digenite and bornite are enriched in Ag, Tl, Hg, Ga, and Se, distributed in the porphyry and epithermal overprinting zone. Enargite and tennantite have high contents of Au, Tl, As, Sb, Sn, Te, Cd, Co, and Bi in the shallow epithermal mineralization zone. These represent a predictive sulfide-metal distribution in overprinted porphyry-epithermal systems, and are of potential interest for exploration.

Supplementary Information The online version contains supplementary material available at https://doi.org/10.1007/s00126-021-01075-y.

Acknowledgements Marc Choquette and Suzie Cote (Université Laval) are thanked for their help with EMPA and SEM analysis. Dany Savard and Audrey Lavoie (UQAC) are thanked for their assistance with LA-ICP-MS analyses and data reduction. We thank Jinlong Mining Co., Ltd. for the support of the fieldwork. The Editor-in-Chief Bernd Lehmann, Associate Editor Peter Hollings, Robert G. Lee, and an anonymous reviewer are acknowledged for their insightful comments, which significantly improved the paper.

Funding This work is supported by the National Key R&D Program of China, Deep Resources Exploration and Mining project (2018YFC0604101), National Natural Science Foundation of China (41902097), the Natural Science and Engineering Research Council of Canada, and the CAS Hundred Talents Program (Y9CJ034000) to XW Huang. The first author's study in Canada is supported by China Scholarship Council (CSC) and NSERC Discovery grant to G. Beaudoin.

References

Brimhall G (1980) Deep hypogene oxidation of porphyry copper potassium-silicate protore at Butte, Montana; a theoretical evaluation of the copper remobilization hypothesis. Econ Geol 75:384–409

Catchpole H, Kouzmanov K, Fontboté L (2012) Copper-excess stannoidite and tennantite-tetrahedrite as proxies for hydrothermal fluid evolution in a zoned Cordilleran base metal district, Morococha, central Peru. Can Mineral 50:719–743

Charlat M, Levy C (1974) Substitutions multiples dans la série tennantite- tétraédrite. Bull Mineral 97:241–250

Chouinard A, Paquette J, Williams-Jones AE (2005) Crystallographic controls on trace-element incorporation in auriferous pyrite from the Pascua epithermal high-sulfidation deposit, Chile-Argentina. Can Mineral 43:951–963

Crespo J, Reich M, Barra F, Verdugo J, Martínez C (2018) Critical metal particles in copper sulfides from the supergiant Río Blanco porphyry Cu–Mo deposit, Chile. Minerals 8. https://doi.org/10.3390/min8110519

Deditius AP, Utsunomiya S, Ewing RC, Chryssoulis SL, Venter D, Kesler SE (2009) Decoupled geochemical behavior of As and Cu in hydrothermal systems. Geology 37:707–710

Deditius AP, Reich M, Kesler SE, Utsunomiya S, Chryssoulis SL, Walshe J, Ewing RC (2014) The coupled geochemistry of Au and As in pyrite from hydrothermal ore deposits. Geochim Cosmochim Acta 140:644–670

Deyell C, Hedenquist J (2011) Trace element geochemistry of enargite in the Mankayan district, Philippines. Econ Geol 106:1465–1478

Duran CJ, Barnes S-J, Corkery JT (2015) Chalcophile and platinum-group element distribution in pyrites from the sulfide-rich pods of the Lac des Iles Pd deposits, Western Ontario, Canada: implications for post-cumulus re-equilibration of the ore and the use of pyrite compositions in exploration. J Geochem Explor 158:223–242

Egozcue JJ, Pawlowsky-Glahn V, Mateu-Figueras G, Barcelo-Vidal C (2003) Isometric logratio transformations for compositional data analysis. Math Geol 35:279–300

Einaudi MT, Hedenquist JW, Inan EE (2003) Sulfidation state of fluids in active and extinct hydrothermal systems: transitions from porphyry to epithermal environments. Soc Econ Geol Spec Pub 10:285–314

Eldridge DL, Guo W, Farquhar J (2016) Theoretical estimates of equilibrium sulfur isotope effects in aqueous sulfur systems: highlighting the role of isomers in the sulfite and sulfoxylate systems. Geochim Cosmochim Acta 195:171–200. https://doi.org/10.1016/j.gca.2016.09.021

Fang X, Tang J, Song Y, Yang C, Ding S, Wang Y-y, Wang Q, Sun X-g, Li Y-b, Wei L-j (2015) Formation epoch of the South Tiegelong superlarge epithermal Cu (Au-Ag) deposit in Tibet and its geological implications. Acta Geosci Sin 36:168–176

Garza RAP, Titley SR, Pimentel F (2001) Geology of the Escondida porphyry copper deposit, Antofagasta region, Chile. Econ Geol 96:307–324

Genna D, Gaboury D (2015) Deciphering the hydrothermal evolution of a VMS system by LA-ICP-MS using trace elements in pyrite: an example from the Bracemac-McLeod eeposits, Abitibi, Canada, and implications for exploratio. Econ Geol 100:2087–2105

George LL, Cook NJ, Ciobanu CL (2017) Minor and trace elements in natural tetrahedrite-tennantite: effects on element partitioning among base metal sulfides. Minerals 7:1–25

Goh SW, Buckley AN, Lamb RN (2006) Copper (II) sulfide? Minerals Eng 19:204–208
Halley S, Dilles J, Tosdal R (2015) Footprints: hydrothermal alteration and geochemical dispersion around porphyry copper deposits. Soc Econ Geol Newsl 100:12–17
He W, Lin B, Yang HH, Fang X, Song YX, Wei SG, Hou L (2017) Fluid inclusion feature and its internal relationship with mineralization and epithermal alteration of the Tiegelongnan Cu-Au deposit. Acta Geosci Sin 38:638–650
He W, Lin B, Yang HH, Song YX (2018) Studies of metallic and trace minerals of the Tiegelongnan Cu-Au deposit, Central Tibet, China. Acta Geol Sin-Engl 92:1123–1138
Heinrich CA, Driesner T, Stefánsson A, Seward TM (2004) Magmatic vapor contraction and the transport of gold from the porphyry environment to epithermal ore deposits. Geology 32:761–764
Huang XW, Boutroy É, Makvandi S, Beaudoin G, Corriveau L, De Toni AF (2019) Trace element composition of iron oxides from IOCG and IOA deposits: relationship to hydrothermal alteration and deposit subtypes. Miner Deposita 54:525–552
Huston DL, Sie SH, Suter GF, Cooke DR, Both RA (1995) Trace elements in sulfide minerals from eastern Australian volcanic-hosted massive sulfide deposits; Part I, Proton microprobe analyses of pyrite, chalcopyrite, and sphalerite, and Part II, Selenium levels in pyrite; comparison with delta 34 S values and implications for the source of sulfur in volcanogenic hydrothermal systems. Econ Geol 90:1167–1196
Kesler SE, Chryssoulis SL, Simon G (2002) Gold in porphyry copper deposits: its abundance and fate. Ore Geol Rev 21:103–124
King J, Williams-Jones A, van Hinsberg V, Williams-Jones G (2014) High-sulfidation epithermal pyrite-hosted Au (Ag-Cu) ore formation by condensed magmatic vapors on Sangihe Island, Indonesia. Econ Geol 109:1705–1733
Kouzmanov K, Pokrovski GS (2012) Hydrothermal controls on metal distribution in porphyry Cu (-Mo-Au) systems. Soc Econ Geol Spec Pub 16:573–618
Landtwing M, Pettke T, Halter W, Heinrich C, Redmond P, Einaudi M, Kunze K (2005) Copper deposition during quartz dissolution by cooling magmatic–hydrothermal fluids: the Bingham porphyry. Earth Planet Sci Lett 235:229–243. https://doi.org/10.1016/j.epsl.2005.02.046
Large RR, Danyushevsky L, Hollit C, Maslennikov V, Meffre S, Gilbert S, Bull S, Scott R, Emsbo P, Thomas H (2009) Gold and trace element zonation in pyrite using a laser imaging technique: implications for the timing of gold in orogenic and Carlin-style sediment-hosted deposits. Econ Geol 104:635–668
Large R, Thomas H, Craw D, Henne A, Henderson S (2012) Diagenetic pyrite as a source for metals in orogenic gold deposits, Otago Schist, New Zealand. New Zeal J Geol Geophys 55:137–149
Li JX, Qin KZ, Li GM, Richards JP, Zhao JX, Cao MJ (2014) Geochronology, geochemistry, and zircon Hf isotopic compositions of Mesozoic intermediate-felsic intrusions in central Tibet: petrogenetic and tectonic implications. Lithos 198–199:77–91. https://doi.org/10.1016/j.lithos.2014.03.025
Li JX, Qin KZ, Li GM, Xiao B, Zhao JX, Chen L (2016) Petrogenesis of Cretaceous igneous rocks from the Duolong porphyry Cu–Au deposit, central Tibet: evidence from zircon U-Pb geochronology, petrochemistry and Sr–Nd–Pb–Hf isotope characteristics. Geol J 51:285–307
Li GM, Qin KZ, Li JX, Evans NJ, Zhao JX, Cao MJ, Zhang XN (2017a) Cretaceous magmatism and metallogeny in the Bangong-Nujiang metallogenic belt, central Tibet: Evidence from petrogeochemistry, zircon U-Pb ages, and Hf-O isotopic compositions. Gondwana Res 41:110–127
Li XK, Li C, Sun ZM, Wang M (2017b) Origin and tectonic setting of the giant Duolong Cu–Au deposit, South Qiangtang Terrane, Tibet: evidence from geochronology and geochemistry of Early Cretaceous intrusive rocks. Ore Geol Rev 80:61–78
Li XK, Chen J, Wang RC, Li C (2018) Temporal and spatial variations of Late Mesozoic granitoids in the SW Qiangtang, Tibet: implications for crustal architecture, Meso-Tethyan evolution and regional mineralization. Earth Sci Rev 185:374–396
Lin B, Chen YC, Tang JX, Wang Q, Song Y, Yang C, Wang WL, He W, Zhang LJ (2017a) 40Ar/39Ar and Rb-Sr ages of the Tiegelongnan porphyry Cu-(Au) deposit in the Bangong Co-Nujiang metallogenic belt of Tibet, China: implication for generation of super-large deposit. Acta Geol Sin-Engl 91:602–616
Lin B, Tang JX, Chen YC, Song Y, Hall G, Wang Q, Yang C, Fang X, Duan JL, Yang HH (2017b) Geochronology and genesis of the Tiegelongnan porphyry Cu (Au) deposit in Tibet: Evidence from U-Pb, Re–Os dating and Hf, S, and H–O isotopes. Resour Geol 67:1–21
Liu D, Huang Q, Fan S, Zhang L, Shi R, Ding L (2014) Subduction of the Bangong-Nujiang Ocean: constraints from granites in the Bangong Co area, Tibet. Geol J 49:188–206
Liu W, Cook NJ, Ciobanu CL, Gilbert SE (2019) Trace element substitution and grain-scale compositional heterogeneity in enargite. Ore Geol Rev 111. https://doi.org/10.1016/j.oregeorev.2019.103004
Makvandi S, Ghasemzadeh-Barvarz M, Beaudoin G, Grunsky EC, Beth McClenaghan M, Duchesne C (2016a) Principal component analysis of magnetite composition from volcanogenic massive sulfide deposits: case studies from the Izok Lake (Nunavut, Canada) and Halfmile Lake (New Brunswick, Canada) deposits. Ore Geol Rev 72:60–85. https://doi.org/10.1016/j.oregeorev.2015.06.023
Makvandi S, Ghasemzadeh-Barvarz M, Beaudoin G, Grunsky EC, McClenaghan MB, Duchesne C, Boutroy E (2016b) Partial least squares-discriminant analysis of trace element compositions of magnetite from various VMS deposit subtypes: application to mineral exploration. Ore Geol Rev 78:388–408
Marcoux E, Milési J, Moëlo Y (1994) Vinciennite and Cu-excess tennantite from the Layo (Cu, Sn, As, Au) epithermal deposit (southern Peru). Mineral Petrol 51:21–36
Maske S, Skinner BJ (1971) Studies of the sulfosalts of copper; I, Phases and phase relations in the system Cu-As-S. Econ Geol 66:901–918
Maydagán L, Franchini M, Lentz D, Pons J, McFarlane C (2013) Sulfide composition and isotopic signature of the Altar Cu-Au deposit, Argentina: constraints on the evolution of the porphyry-epithermal system. Can Mineral 51:813–840
Maydagán L, Franchini M, Rusk B, Lentz DR, McFarlane C, Impiccini A, Ríos FJ, Rey R (2015) Porphyry to epithermal transition in the Altar Cu-(Au-Mo) deposit, Argentina, studied by cathodoluminescence, LA-ICP-MS, and fluid inclusion analysis. Econ Geol 110:889–923
Ossandón G, Gustafson LB, Lindsay DD, Zentilli M (2001) Geology of the Chuquicamata mine: a progress report. Econ Geol 96:249–270
Pacevski A, Libowitzky E, Zivkovic P, Dimitrijevic R, Cvetkovic L (2008) Copper-bearing pyrite from the Coka Marin polymetallic deposit, Serbia: mineral inclusions or true solid-solution? Can Mineral 46:249–261. https://doi.org/10.3749/canmin.46.1.249
Pan G, Wang L, Li R, Yuan S, Ji W, Yin F, Zhang W, Wang B (2012) Tectonic evolution of the Qinghai-Tibet plateau. J Asian Earth Sci 53:3–14
Paton C, Hellstrom J, Paul B, Woodhead J, Hergt J (2011) Iolite: Freeware for the visualisation and processing of mass spectrometric data. J Anal At Spectrom 26. https://doi.org/10.1039/c1ja10172b
Pearce C, Pattrick R, Vaughan D, Henderson C, Van der Laan G (2006) Copper oxidation state in chalcopyrite: mixed Cu d9 and d10 characteristics. Geochim Cosmochim Acta 70:4635–4642

Pokrovski GS, Zakirov IV, Roux J, Testemale D, Hazemann J-L, Bychkov AY, Golikova GV (2002) Experimental study of arsenic speciation in vapor phase to 500 C: Implications for As transport and fractionation in low-density crustal fluids and volcanic gases. Geochim Cosmochim Acta 66:3453–3480

Pokrovski GS, Roux J, Harrichoury J-C (2005) Fluid density control on vapor-liquid partitioning of metals in hydrothermal systems. Geology 33. https://doi.org/10.1130/g21475.1

Posfai M, Buseck PR (1998) Relationships between microstructure and composition in enargite and luzonite. Am Mineral 83:373–382

Redmond PB, Einaudi MT (2010) The Bingham canyon porphyry Cu-Mo-Au deposit. I. Sequence of intrusions, vein formation, and sulfide deposition. Econ Geol 105:43–68

Redmond P, Einaudi M, Inan E, Landtwing M, Heinrich C (2004) Copper deposition by fluid cooling in intrusion-centered systems: new insights from the Bingham porphyry ore deposit, Utah. Geology 32:217–220

Reich M, Kesler SE, Utsunomiya S, Palenik CS, Chryssoulis SL, Ewing RC (2005) Solubility of gold in arsenian pyrite. Geochim Cosmochim Acta 69:2781–2796. https://doi.org/10.1016/j.gca.2005.01.011

Reich M, Chryssoulis SL, Deditius A, Palacios C, Zuniga A, Weldt M, Alvear M (2010) "Invisible" silver and gold in supergene digenite (Cu1.8S). Geochim Cosmochim Acta 74:6157–6173

Reich M, Deditius A, Chryssoulis S, Li JW, Ma CQ, Parada MA, Barra F, Mittermayr F (2013) Pyrite as a record of hydrothermal fluid evolution in a porphyry copper system: a SIMS/EMPA trace element study. Geochim Cosmochim Acta 104:42–62

Rottier B, Kouzmanov K, Wälle M, Bendezú R, Fontboté L (2016) Sulfide replacement processes revealed by textural and LA-ICP-MS trace element analyses: example from the early mineralization stages at Cerro de Pasco, Peru. Econ Geol 111:1347–1367

Rottier B, Kouzmanov K, Casanova V, Wälle M, Fontboté L (2018) Cyclic dilution of magmatic metal-rich hypersaline fluids by magmatic low-salinity fluid: a major process generating the giant epithermal polymetallic deposit of Cerro de Pasco, Peru. Econ Geol 113:825–856. https://doi.org/10.5382/econgeo.2018.4573

Rye RO (1993) The evolution of magmatic fluids in the epithermal environment; the stable isotope perspective. Econ Geol 88:733–752

Rye RO, Ohmoto H (1974) Sulfur and carbon isotopes and ore genesis: a review. Econ Geol 69:826–842

Seo JH, Guillong M, Heinrich CA (2009) The role of sulfur in the formation of magmatic–hydrothermal copper–gold deposits. Earth Planet Sci Lett 282:323–328. https://doi.org/10.1016/j.epsl.2009.03.036

Seward TM (1973) Thio complexes of gold and the transport of gold in hydrothermal ore solutions. Geochim Cosmochim Acta 37:379–399

Sillitoe RH (2010) Porphyry copper systems. Econ Geol 105:3–41

Sillitoe RH (1999) Styles of high-sulphidation gold, silver and copper mineralisation in porphyry and epithermal environments. In Weber G (ed) Pacrim '99 Congress, Bali, Indonesia, 1999, Proceedings: Parkville, Australasian Institute of Mining and Metallurgy: 29–44

Simmons SF, Brown KL, Tutolo BM (2016) Hydrothermal transport of Ag, Au, Cu, Pb, Te, Zn, and other metals and metalloids in New Zealand geothermal systems: spatial patterns, fluid-mineral equilibria, and implications for epithermal mineralization. Econ Geol 111:589–618

Simon G, Kesler SE, Essene EJ, Chryssoulis SL (2000) Gold in porphyry copper deposits: Experimental determination of the distribution of gold in the Cu-Fe-S system at 400 to 700 C. Econ Geol 95:259–270

Song Y, Yang C, Wei SG, Yang HH, Fang X, Lu HT (2018) Tectonic control, reconstruction and preservation of the Tiegelongnan porphyry and epithermal overprinting Cu (Au) deposit, Central Tibet, China. Minerals 8:398–415. https://doi.org/10.3390/min8090398

Sun J, Mao J, Beaudoin G, Duan X, Yao F, Ouyang H, Wu Y, Li Y, Meng X (2017) Geochronology and geochemistry of porphyritic intrusions in the Duolong porphyry and epithermal Cu-Au district, central Tibet: Implications for the genesis and exploration of porphyry copper deposits. Ore Geol Rev 80:1004–1019

Sykora S, Cooke DR, Meffre S, Stephanov AS, Gardner K, Scott R, Selley D, Harris AC (2018) Evolution of pyrite trace element compositions from porphyry-style and epithermal conditions at the Lihir gold deposit: implications for ore genesis and mineral processing. Econ Geol 113:193–208

Tang J, Sun X, Ding S, Wang Q, Wang Y, Yang C, Chen H, Li Y, Li Y, Wei L (2014) Discovery of the epithermal deposit of Cu (Au-Ag) in the Duolong ore concentrating area, Tibet. Acta Geosci Sin 35:6–10

Tang JX, Wang Q, Yang HH, Gao X, Zhang ZB, Zou B (2017) Mineralization, exploration and resource potential of porphyry-skarn-epithermal copper polymetallic deposits in Tibet. Acta Geosci Sin 38:571–613

Wang Q, Tang JX, Fang X, Lin B, Song Y, Wang YY, Yang HH, Yang C, Li Y, Wei LJ (2015) Petrogenetic setting of andsites in Rongna ore block, Tiegelong Cu (Au–Ag) deposit, Duolong ore concentration area, Tibet: evidence from zircon U-Pb LA–ICP–MS dating and petrogeochemistry of andsites. Chin Geol 42:1324–1336

Wang YY, Tang JX, Song Y, Yang C, Lin B, Wang Q, Sun M, Gao K, Fang X, Yang HH (2018) Characteristics of the main ore minerals in Tiegelongnan porphyry-high sulfidation deposit, Tibet, China. Acta Min Sin 38:109–122

Wei SG, Tang JX, Song Y, Liu ZB, Feng J, Li YB (2017) Early Cretaceous bimodal volcanism in the Duolong Cu mining district, western Tibet: Record of slab breakoff that triggered ca. 108–113 Ma magmatism in the western Qiangtang terrane. J Asian Earth Sci 138:588–607

Wilson S, Ridley W, Koenig A (2002) Development of sulfide calibration standards for the laser ablation inductively-coupled plasma mass spectrometry technique. J Anal at Spectrom 17:406–409

Wu YF, Evans K, Li JW, Fougerouse D, Large RR, Guagliardo P (2019a) Metal remobilization and ore-fluid perturbation during episodic replacement of auriferous pyrite from an epizonal orogenic gold deposit. Geochim Cosmochim Acta 245:98–117. https://doi.org/10.1016/j.gca.2018.10.031

Wu YF, Fougerouse D, Evans K, Reddy SM, Saxey DW, Guagliardo P, Li JW (2019b) Gold, arsenic, and copper zoning in pyrite: a record of fluid chemistry and growth kinetics. Geology. https://doi.org/10.1130/g46114.1

Xie Y, Riedinger A, Prato M, Casu A, Genovese A, Guardia P, Sottini S, Sangregorio C, Miszta K, Ghosh S, Pellegrino T, Manna L (2013) Copper sulfide nanocrystals with tunable composition by reduction of covellite nanocrystals with Cu+ ions. J Am Chem Soc 135:17630–17637. https://doi.org/10.1021/ja409754v

Yang C, Tang J, Wang Y, Yang H, Wang Q, Sun X, Feng J, Yin X, Ding S, Fang X (2014) Fluid and geological characteristics researches of Southern Tiegelong epithermal porphyry Cu-Au deposit in Tibet. Mineral Deposits 33:1287–1305

Yang C, Tang J, Beaudoin G, Song Y, Lin B, Wang Q, Fang X (2020) Geology and geochronology of the Tiegelongnan porphyry-epithermal Cu (Au) deposit, Tibet, China: formation, exhumation and preservation history. Ore Geol Rev 123:103575

Yang C, Beaudoin G, Tang J-X, Song Y, Zhang Z (2020a) Hydrothermal fluid evolution at the Tiegelongnan porphyry-epithermal Cu(Au) deposit, Tibet, China: Constraints from H and O stable isotope and in-situ S isotope. Ore Geol Rev 125. https://doi.org/10.1016/j.oregeorev.2020.103694

Yin A, Harrison TM (2000) Geologic evolution of the Himalayan-Tibetan orogen. Annu Rev Earth Planet Sci 28:211–280

Zhang KJ, Zhang YX, Tang XC, Xia B (2012) Late Mesozoic tectonic evolution and growth of the Tibetan plateau prior to the Indo-Asian collision. Earth Sci Rev 114:236–249

Zhang Z, Yao XF, Tang JX, Li ZJ, Wang LQ, Yang Y, Duan JL, Song JL, Lin X (2015) Lithogeochemical, Re-Os and U-Pb geochronological, Hf-Lu and S-Pb isotope data of the Ga'erqiong-Galale Cu-Au ore concentrated area: evidence for the Late Cretaceous magmatism and metallogenic event in the Bangong-Nujiang Suture Zone, Northwestern Tibet, China. Resour Geol 65:76–102

Zhang XN, Li GM, Qin KZ, Lehmann B, Li JX, Zhao JX, Cao MJ, Zou XY (2018) Petrogenesis and tectonic setting of Early Cretaceous granodioritic porphyry from the giant Rongna porphyry Cu deposit, central Tibet. J Asian Earth Sci 161:74–92

Zhang XN, Li GM, Qin KZ, Lehmann B, Li JX, Zhao JX (2020) Porphyry to epithermal transition at the Rongna Cu-(Au) deposit, Tibet: insights from HO isotopes and fluid inclusion analysis. Ore Geol Rev 123:103585

Zhu DC, Li SM, Cawood PA, Wang Q, Zhao ZD, Liu SA, Wang LQ (2016) Assembly of the Lhasa and Qiangtang terranes in central Tibet by divergent double subduction. Lithos 245:7–17